EARTH SURFACE PROCESSES AND LANDFORMS
Earth Surf. Process. Landforms **36,** 117–135 (2011)

Published online 20 October 2010 in Wiley Online Library
(wileyonlinelibrary.com) DOI: 10.1002/esp.2083

The sensitivity of hillslope bedrock erosion to precipitation

Justine J. Owen,[1]* Ronald Amundson,[1] William E. Dietrich,[2] Kunihiko Nishiizumi,[3] Brad Sutter[4] and Guillermo Chong[5]
[1] Department of Environmental Science, Policy & Management, University of California, Berkeley, CA, USA
[2] Department of Earth and Planetary Science, University of California, Berkeley, CA, USA
[3] Space Science Laboratory, University of California, Berkeley, CA, USA
[4] NASA, Johnson Space Center, Houston, TX, USA
[5] Departamento de Ciencias Geológicas, Unversidad Católica del Norte, Antofagasta, Chile

Received 19 August 2009; Revised 21 July 2010; Accepted 26 July 2010

*Correspondence to: Justine J. Owen, Department of Environmental Science, Policy & Management, University of California, Berkeley, CA, USA. E-mail: justineosaur@gmail.com

ESPL
Earth Surface Processes and Landforms

ABSTRACT: Decoupling the impacts of climate and tectonics on hillslope erosion rates is a challenging problem. Hillslope erosion rates are well known to respond to changes in hillslope boundary conditions (e.g. channel incision rates) through their dependence on soil thickness, and precipitation is an important control on soil formation. Surprisingly though, compilations of hillslope denudation rates suggest little precipitation sensitivity. To isolate the effects of precipitation and boundary condition, we measured rates of soil production from bedrock and described soils on hillslopes along a semi-arid to hyperarid precipitation gradient in northern Chile. In each climate zone, hillslopes with contrasting boundary conditions (actively incising channels versus non-eroding landforms) were studied.

Channel incision rates, which ultimately drive hillslope erosion, varied with precipitation rather than tectonic setting throughout the study area. These precipitation-dependent incision rates are mirrored on the hillslopes, where erosion shifts from relatively fast and biologically-driven to extremely slow and salt-driven as precipitation decreases. Contrary to studies in humid regions, bedrock erosion rates increase with precipitation following a power law, from ~1 m Ma^{-1} in the hyperarid region to ~40 m Ma^{-1} in the semi-arid region. The effect of boundary condition on soil thickness was observed in all climate zones (thicker soils on hillslopes with stable boundaries compared to hillslopes bounded by active channels), but the difference in bedrock erosion rates between the hillslopes within a climate region (slower erosion rates on hillslopes with stable boundaries) decreased as precipitation decreased. The biotic-abiotic threshold also marks the precipitation rate below which bedrock erosion rates are no longer a function of soil thickness. Our work shows that hillslope processes become sensitive to precipitation as life disappears and the ability of the landscape to respond to tectonics decreases. Copyright © 2010 John Wiley & Sons, Ltd.

KEYWORDS: erosion; climate; hillslope; cosmogenic radionuclides; Atacama

Introduction

How does precipitation affect the mechanisms and rates of geomorphic processes, particularly those driving bedrock erosion, on soil-mantled, non-landsliding hillslopes? The imprint of precipitation and biota on soil formation processes has long been recognized (e.g. Jenny, 1941, and references cited therein), but only recently have the rates of hillslope soil production and transport been quantifiable using cosmogenic radionuclides (CRN). Despite a growing database of CRN-derived denudation rates (denudation rate is the rate of physical and chemical erosion, equal to the rate of soil production from bedrock when soil mass is at steady state), evidence of precipitation-dependence remains elusive. Riebe *et al*. (2004a) found that 42 denudation rates for 14 gentle, non-glaciated hillslopes spanning a broad spectrum of mean annual temperature (MAT: 2–25 °C) and mean annual precipitation (MAP: 250–4200 mm) were not correlated with MAP or MAT. In another compilation, von Blanckenburg (2006) found catchment-averaged denudation rates (calculated using stream sediment CRN) at sites worldwide were independent of MAP and MAT.

No clear linkage between denudation rate and MAP or MAT has been observed, and large variations in the measured denudation rates in any given climate suggest that other factors, such as tectonics, bedrock characteristics (particularly fracturing), and the co-variation of precipitation and temperature, may obscure the precipitation signal. Riebe *et al*. (2001) found that hillslopes bounded by faulting-affected river canyons erode faster compared to hillslopes bounded by low-relief surfaces (indicative of less incision). They concluded that tectonic uplift, through its effect on channel incision rates (i.e. local boundary condition) and subsequent hillslope response, is the primary control on

denudation rates. This was confirmed by von Blanckenburg (2006) who showed that variation in tectonic setting (affecting hillslopes through channel incision response to uplift) obscures any MAP or MAT signal. Alternatively, Molnar *et al*. (2007) argue that it is not the uplift rate but the disintegration of bedrock due to tectonic stresses that influences erosion rates. In that vein, Selby (1980) proposed a classification system for rock mass strength to address the effect of jointing and residual stress on hillslope geomorphology. Hillslope erosion may also be bedrock-dependent due to small variations in mineralogy or grain size (e.g. Onda, 1992). However, no study has attempted to account for degree of fracturing or grain size in addition to precipitation and boundary condition. MAT may obscure the role of MAP, particularly when elevation gradients are used to create climosequences (e.g. Riebe *et al*., 2004b; Dixon *et al*., 2009). MAP and MAT often vary inversely with elevation and so their individual effects upon process rates are difficult to separate (e.g. Dahlgren *et al*., 1997). Without careful site selection, teasing apart the effects of precipitation, temperature, bedrock characteristics, and boundary condition may be difficult.

Here we examine hillslopes in northern Chile at the dry end of the Earth's precipitation spectrum to quantify the response of hillslope processes to increasing aridity and differing boundary conditions. This study was motivated by our observations of large variations in soil thickness and chemistry (Ewing *et al*., 2006) along the precipitation gradient in this region, particularly at the threshold for plant growth. We studied pairs of hillslopes along a precipitation gradient which had similar bedrock types, uplift rates, and MAT. Each pair had one hillslope responding to active channel incision and one responding to a non-eroding surface. We measured the thickness and chemical nature of the soil mantle, identified the mechanisms of bedrock erosion and soil transport, and quantified bedrock erosion rates (the rates of hillslope soil production from bedrock and local channel incision rates). Our observations reveal systematic differences in soil thickness and bedrock erosion due to boundary condition, as expected from geomorphic models but, in contrast to previous work (Riebe *et al*., 2004a; von Blanckenburg, 2006), bedrock erosion rate decreases with decreasing MAP. This decrease coincides with changes in the mechanisms of soil production and transport. When compared with work in more humid settings, a critical MAP-threshold appears to exist below which bedrock erosion is MAP-dependent and above which soil production from bedrock is controlled by the complex interaction of other factors including tectonic uplift, biota, and MAT.

Theoretical Framework

The relationship between hillslope soil processes, boundary conditions, and precipitation can be approached through a mass balance. Here we outline the components of the mass balance and their potential responses to boundary conditions and precipitation. Throughout this paper, 'soil' refers to the physically disrupted, chemically altered material that lacks relict bedrock structure (bedding, foliation, etc.) and is subject to downslope transport; 'saprolite' is bedrock that has been sufficiently weathered such that it has become a soil-like material (in strength and chemical alteration) but has relict rock structure and has not been physically transported; and 'weathered rock' refers to bedrock that shows some signs of physical and/or chemical alteration, but is mechanically resistant.

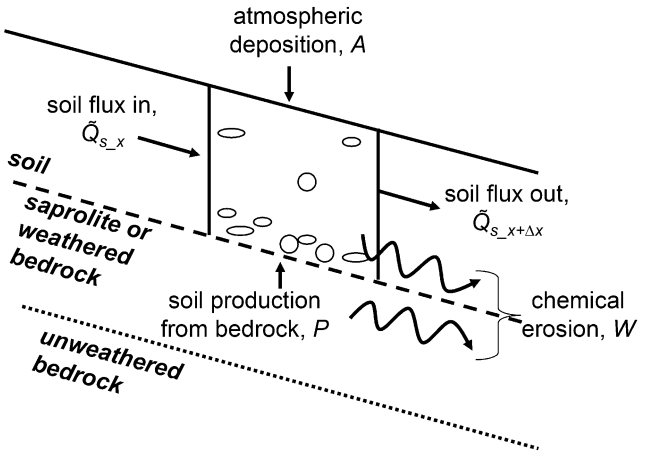

Figure 1. A diagram of a hillslope soil profile showing inputs and outputs as described in Equation 1. Soil production from bedrock can be calculated using cosmogenic radionuclides if the soil is at steady state (i.e. production from bedrock and soil mass have been constant).

Hillslope soil mass balance and the soil production function

The mass of the hillslope soil mantle is determined by the balance between soil erosion and soil production (Figure 1). This can be expressed as the difference between soil inputs and outputs per unit area of hillslope:

$$\frac{\partial(\rho_s h)}{\partial t} = \underbrace{\underbrace{\rho_r P}_{\substack{\text{production}\\ \text{from}\\ \text{bedrock}}} + \underbrace{A}_{\substack{\text{atmospheric}\\ \text{deposition}}}}_{\substack{\text{soil production}\\ \text{mechanisms}}} - \underbrace{\underbrace{\nabla\cdot\tilde{Q}_s}_{\substack{\text{physical}\\ \text{erosion}}} - \underbrace{W}_{\substack{\text{chemical}\\ \text{erosion}}}}_{\substack{\text{soil loss}\\ \text{mechanisms}}} \quad (1)$$

where ρ_s is the soil bulk density (M L^{-3}), h is the vertical soil thickness (L), ρ_r is the bedrock bulk density (M L^{-3}), P is the bedrock erosion rate (L T^{-1}), A is the deposition rate of silicate dust and salts from the atmosphere (M L^{-2} T^{-1}), $\nabla\cdot\tilde{Q}_s$ is the rate of physical erosion (the divergence of soil flux, Q_s) (M L^{-2} T^{-1}), and W is the rate of chemical erosion (M L^{-2} T^{-1}). Here P is called the 'bedrock erosion rate' rather than the 'soil production rate' because both P and A are rates of soil production. Chemical erosion of bedrock (Anderson *et al*., 2002; Dixon *et al*., 2009; Lebedeva *et al*., 2010) is not considered here.

Hillslopes evolve in response to channel incision at their base, the rate of which defines a 'boundary condition' which can drive hillslope erosion rates. A slope-dependent soil transport law, $Q_s = f(\nabla z)$ where ∇z is slope, enables 'communication' between the boundary condition at the base of the slope and the soils upslope from it (e.g. Fernandes and Dietrich, 1997). The expression for Q_s reflects the erosion processes involved and may include a combination of the following expressions (Braun *et al*., 2001). Soil creep (e.g. freeze–thaw and shrink–swell) and biologically-driven transport (e.g. tree throw and animal burrowing) are either a function of slope, $Q_s = -K\nabla z$, or of the depth-slope product, $Q_s = -K_h H\nabla z$ (where K and K_h are empirical 'transport coefficients' and H is the slope-normal soil thickness, equal to $h\cos\theta$) (Heimsath *et al*., 1997; Heimsath *et al*., 2005; Heimsath *et al*., 2006; Braun *et al*., 2001; Yoo *et al*., 2007). On sufficiently steep slopes, soil flux may increase non-linearly with slope (e.g. Roering *et al*., 1999; Roering, 2008). Where overland flow is important, soil flux is also a function of drainage area (or distance from the upslope divide). Transport laws for this process are less established, but

$Q_s = -K_w A^m \nabla z^n$ is commonly assumed, where A is upslope area and K_w, m, and n are empirical constants (e.g. Dietrich *et al*., 2003). In any of these cases, an increase in slope increases soil flux and the more negative the hillslope curvature ($\nabla^2 z$, where positive is concave and negative is convex) the greater the physical erosion rate. Where curvature is zero (i.e. ∇z is constant), soil flux is constant and where curvature is positive there is deposition rather than erosion.

Increased erosion will thin the soil, which will tend to increase P (Dietrich *et al*., 2003; Dietrich and Perron, 2006). The hypothesis that P varies inversely with soil thickness originated with Gilbert (1877), and CRN-derived rates of P in California and Australia (Heimsath *et al*., 1997, 1999; Heimsath *et al*., 2000; Wilkinson and Humphreys, 2005) demonstrate that P decreases exponentially with increasing H:

$$P = P_0 e^{-\alpha H} \tag{2}$$

where P_0 is the bedrock erosion rate under zero soil cover and α is an empirical rate constant. Equation 2 (the soil production function) predicts that bare bedrock has the highest P. A 'humped' function, with maximum P at some critical soil thickness (Carson and Kirkby, 1972; Dietrich *et al*., 1995; Furbish and Fagherazzi, 2001; Anderson, 2002), may be more reasonable, in that some soil is required to store water, support plants, and harbor burrowing animals, all of which increase P. Work in Australia (Heimsath *et al*., 2006; Heimsath *et al*., 2009), South Africa (Heimsath *et al*., 2008), and Wyoming (Small *et al*., 1999) supports the humped function.

Regardless of the 'shape' of the soil production function, the combination of depth-dependent bedrock erosion and slope-dependent soil flux produces a feedback between physical erosion and P such that P is sensitive to varying channel incision rates. If incision rates increase at the hillslope boundary, steepening slopes will increase physical erosion, thinning the soil, increasing P, and driving soil erosion, hillslope form, and soil thickness to a new equilibrium (e.g. Dietrich *et al*., 1995). Modeling experiments incorporating slope-dependent soil flux (but not depth-dependent P) illustrate the impact of downslope boundary conditions on the shape of the hillslope (Kirkby, 1971; Ahnert, 1987; Armstrong, 1987; Anderson and Humphrey, 1989; Fernandes and Dietrich, 1997). Other models include the effects of soil thickness on hillslope response (e.g. Ahnert, 1970; Furbish and Fagherazzi, 2001; Furbish, 2003; Mudd and Furbish, 2004; Mudd and Furbish, 2007). These models show that a constant incision rate can produce steady-state soil thicknesses at upslope positions, whereas the cessation of incision leads to progressive upslope deviation from steady state.

Precipitation is not explicitly expressed in the equations shown earlier. However, it likely influences K in the soil flux equations, a constant that may also incorporate geologic and biotic effects. In the soil production function, P_0 should mostly depend on bedrock characteristics but could be sensitive to precipitation, as could α. An interesting question is how precipitation (and resulting biota) impacts K, P_0, and α, and how these might affect W (Riebe *et al*., 2004a; Dixon *et al*., 2009), but that is beyond the scope of this work.

Cosmogenic radionuclide analysis

CRNs are produced near the Earth's surface by cosmic rays, and the rate of production decreases exponentially with increasing depth. CRNs produced *in situ* in rock are used to calculate bedrock denudation rates, determine if local soil mass has been constant, and constrain the age of land surfaces (e.g. Lal, 1991). The concentration of a CRN, C (atom g^{-1}), in a rock reflects the time during which it has been near the surface, and is controlled by the rates of erosion and deposition above it. At depth H (in centimeters), if the CRN production rate at the surface (P_{CRN}, in atom g^{-1} a^{-1}), and bedrock erosion rate (P, cm a^{-1}, equivalent to P in Equation 1), are constant, then

$$C(H) = P_{CRN} e^{-\frac{\rho_s H}{\Lambda}} \left(\frac{1}{\lambda + \frac{\rho_r P}{\Lambda}} \right) \left(1 - e^{-\left(\lambda + \frac{\rho_r P}{\Lambda}\right) t} \right) \tag{3}$$

where λ is the CRN decay constant (in a^{-1}), ρ_s is the bulk density of the soil or overlying material (in g cm^{-3}), Λ is the mean attenuation length of cosmic ray interaction (in g cm^{-2}), ρ_r is the bedrock bulk density (in g cm^{-3}), and t is the cosmic ray exposure time (unit of time used *annus*, a) (e.g. Lal and Arnold, 1985; Lal, 1991). This calculation assumes no inherited CRN and negligible muon contribution.

P is often called the 'denudation rate' because, if A (Equation 1) is ignored, a steady-state soil mass balance ($\partial(\rho_s h)/\partial t = 0$) requires that P is equal to the rate of soil loss ($\nabla \cdot \tilde{Q}_s + W$ in Equation 1). In this paper, because of the influence of A, we avoid using 'denudation rate' and refer to the erosion rate calculated from CRN concentrations as the bedrock erosion rate. At steady state, weathering of rock (e.g. saprolitization) should keep pace with bedrock erosion. However, we have no measurements or observations as to whether this is occurring in our field areas.

For a continuous, long-term cosmic ray irradiation [$t >> (\lambda + \rho_r P \Lambda^{-1})^{-1}$], and constant erosion, Equation 3 reduces to:

$$C = P_{CRN} e^{-\frac{\rho_s H}{\Lambda}} \left(\frac{1}{\lambda + \frac{\rho_r P}{\Lambda}} \right) \tag{4}$$

which can be rearranged to solve for P:

$$P = \frac{\Lambda}{\rho_r} \left(\frac{P_{CRN} e^{-\frac{\rho_s H}{\Lambda}}}{C} - \lambda \right) \tag{5}$$

P calculated from Equation 5 is a maximum erosion rate because it assumes long-term irradiation of the sample by cosmic rays.

Pairs of CRN, such as aluminum-26 (^{26}Al) and beryllium-10 (^{10}Be) produced in quartz, are often analyzed because they have different response times to perturbations in steady-state conditions. A comparison of their concentrations in a sample can, under certain conditions, reveal deviation from steady state that would not be recognized with a single nuclide. In quartz, the production rate ratio, R_0, of ^{26}Al and ^{10}Be is 6·7 (Nishiizumi *et al*., 1989, revised in Nishiizumi *et al*., 2007). At steady state, the ratio of their concentrations in the sample, $R = {}^{26}\text{Al}/{}^{10}\text{Be}$, can be derived from Equation 4,

$$\frac{C_{^{26}Al}}{C_{^{10}Be}} = R = R_0 \left(\frac{\lambda_{^{10}Be} + \frac{\rho_r P}{\Lambda}}{\lambda_{^{26}Al} + \frac{\rho_r P}{\Lambda}} \right) \tag{6}$$

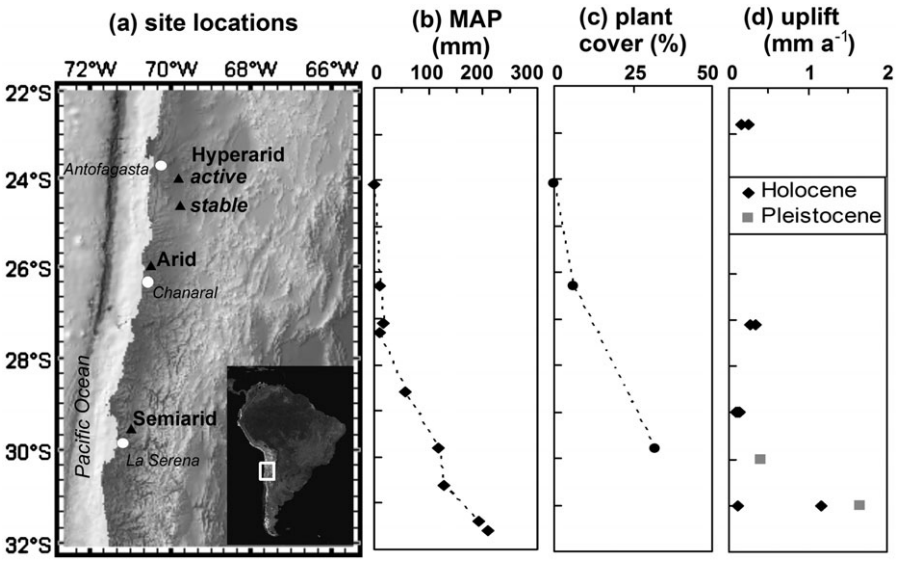

Figure 2. (a) A shaded relief map showing site locations as black triangles (created with GeoMapApp v.1.7.8). Only in the hyperarid region were the two hillslopes sufficiently apart (~70 km) to necessitate separate markers on the map. Nearby towns are marked with white dots. (b) Mean annual precipitation (MAP) increases with longitude (Worldclimate.com, accessed November 18, 2009). (c) Plant density (measured in this study) follows MAP and increases with latitude. (d) Coastal uplift rates have been uniform across the study area in the Holocene. Uplift data compiled from Leonard and Wehmiller (1992), Ota *et al*. (1995), Ortlieb *et al*. (1996), Marquardt *et al*. (2004), Le Roux *et al*. (2005, 2006), Encinas *et al*. (2006), Quezada *et al*. (2007), and Saillard *et al*. (2009).

Rearranged, Equation 6 can be used to calculate P:

$$P = \frac{\Lambda}{\rho_r}\left(\frac{R\lambda_{^{26}\mathrm{Al}} - R_0\lambda_{^{10}\mathrm{Be}}}{R_0 - R}\right) \quad (7)$$

R decreases with decreasing P and increasing cosmic ray exposure time, t, reaching a minimum of 3·5 when bedrock erosion is zero and exposure is longer than the half-life of ^{10}Be. This is illustrated on a ^{10}Be-^{26}Al/^{10}Be plot, in which the upper boundary of an 'erosion window' is defined by the evolution of ^{26}Al/^{10}Be over time with zero erosion, and the window's lower boundary by steady-state C for a range of erosion rates (illustrated in the Results section). If the ratio of a sample plots below the erosion window, then the sample has experienced a complex exposure history ($\partial h/\partial t \neq 0$ or $\partial P/\partial t \neq 0$) or there is experimental error (e.g. Lal, 1991; Nishiizumi *et al*., 1991). Although a sample's exposure history cannot be completely resolved with only two nuclides, Equations 5 and 7 can be used to better constrain it. If a sample was exposed to cosmic rays under constant erosion for sufficient time, the P values obtained from Equations 5 and 7 are the same. At low erosion rates (higher CRN concentration), P values calculated from Equation 5 have larger uncertainty because the calculation is more sensitive to uncertainty in C. At high erosion rates (lower CRN concentration), P calculated from Equation 7 have larger uncertainty because R is closer to R_0. Discretion is required to interpret data from slowly eroding, ancient landscapes.

The minimum exposure age of a sample can be calculated from Equation 3 if there is no inheritance of CRN, no erosion ($P = 0$), and simple exposure:

$$t = -\frac{1}{\lambda}\ln\left(1 - \frac{C\lambda}{P_{\mathrm{CRN}}}\right) \quad (8)$$

This approach has been used extensively to calculate the ages of stable landforms (e.g. Nishiizumi *et al*., 2005). Potential complications include the movement of the target material on the surface and non-zero erosion which may produce a non-zero initial CRN content or change the orientation of the rock to cosmic ray flux. Field observations and the evaluation of ^{26}Al/^{10}Be isochrones can often determine if these complications are significant.

Study Area

Northern Chile (Figure 2a) was selected for our study because a long-term precipitation gradient exists over a region with spatially-uniform uplift and areas of similar bedrock. The Atacama Desert is primarily located in a north-south trending valley, the Central Depression, bounded on the west by the Coastal Cordillera and on the east by the pre-Andean ranges. The Central Depression becomes increasingly discontinuous south of about 26°S, though the general features of the Coastal Cordillera and pre-Andean ranges remain in place (Mortimer, 1973). The southern boundary of the Atacama is subject to debate. Rundel *et al*. (1991) suggest the present-day border lies near 30°S based on a shift in vegetation from semi-arid coastal scrub to succulent desert plants, but the nearly lifeless zone for which the Atacama is renowned ends near 26·3°S.

Climate and biota

Present-day coastal MAP decreases exponentially with decreasing latitude (Ericksen, 1981) (Figure 2b). South of ~21°S, winter Pacific Westerlies are the source of rainfall to the Coast Range and Central Depression, whereas north of ~21°S the summer Atlantic Easterlies are the main source (Houston, 2006). Regardless of its source, rainfall in the Central Depression may fail to occur for decades (Ericksen, 1981; Vargas *et al*. 2006). Fog is a significant source of moisture at elevations below ~1000 m near the coast (Rundel *et al*., 1991). Geochemical evidence suggests that dry conditions have persisted at least periodically since the middle to late Miocene (Alpers and Brimhall, 1988; Sillitoe and McKee, 1996; Hartley and Chong, 2002; Dunai *et al*., 2005; Nishiizumi *et al*., 2005; Clarke, 2006; Houston, 2006; Kober *et al*., 2007), and possibly much earlier (Hartley *et al*., 2005; Clarke, 2006; Evenstar *et al*., 2009). Research in the southern Pacific suggests that the present Pacific circulation (El Niño-Southern Oscillation, ENSO) was emplaced near the end of the Pliocene (Ravelo *et al*., 2004) and may signal the onset of the present episode of hyperaridity.

Within this long (>2 Ma) period of aridity have been episodes of more pluvial conditions. Offshore sediment deposits between 24°S and 44°S indicate that the position of the Southern Westerlies has occasionally moved north as much as 5° latitude from its current position during the last 80 ka (Lamy *et al*., 2000; Hebbeln *et al*., 2007). Other short-term variations

have been recorded in paleowetland deposits (Rech *et al*., 2003) and rodent middens (Betancourt *et al*., 2000; Latorre *et al*., 2002; Latorre *et al*., 2003). In the northern part of the Atacama Desert, these periods of greater precipitation have been of insufficient magnitude and duration to remove or chemically alter highly water-soluble and biologically-reactive compounds such as nitrate, which have been accumulating since the early Pliocene (Ewing *et al*., 2007). Thus, present regional trends in rainfall are indicative of post-Pliocene climate conditions (generally more arid).

In the Central Depression and Coastal Cordillera, systematic changes in biota occur with latitude due to the changes in MAP (Figure 2c). The hyperarid north (~19°–23°S) is a nearly abiotic landscape (Navarro-González *et al*., 2003; Warren-Rhodes *et al*., 2006) with no vascular plants. Biota increases with increasing latitude, such that scattered fog-adapted plants appear around 26°S, and a succulent desert scrub ecosystem is present by ~29°S (Rundel *et al*., 1991).

Geologic setting

Bedrock in the Atacama Desert is a complex mixture of volcanic, plutonic, and metasedimentary rock due to multiple volcanic episodes and long-term plate convergence (Ericksen, 1981). The Atacama Gravels blanket much of the region from the foothills of the pre-Andean ranges, through the Central Depression, and into the Coastal Cordillera. They are a widely-distributed, thick sequence of fluvial sediments and tuff interbeds, deposited beginning in the Oligocene with the onset of Andean uplift and through the late Miocene (Ericksen, 1981). Up to several hundred meters of this sediment has been locally removed since the Miocene, but Quaternary reworking of sediment is extremely limited despite continuing regional uplift (Figure 2d). Many low hills (<200 m relief) in the Central Depression, possibly including the hillslopes at the north end of our study transect, were likely completely or partially buried by the Atacama Gravels and have been re-exposed by post-Miocene erosion (Nester, 2008). However, arid conditions have limited erosion (see later), therefore, the general shapes of some hillslopes, particularly in the hyperarid core of the desert, were likely achieved in the Miocene or earlier and have since been only slightly altered. Many topographic features are likely relicts of a wetter past that are being slowly reworked under arid to hyperarid conditions.

Landform change since the Miocene has been remarkably slow. CRN-derived calculations of bedrock and boulder erosion rates in the northern pre-Andean range and throughout the Atacama are generally <2 m Ma^{-1} but increase more than two-orders of magnitude with increasing elevation (i.e. precipitation) (Kober *et al*., 2007; Nishiizumi *et al*., 2005; Placzek *et al*., 2010). Boulders provide a minimum erosion rate for the landscape because bare rock outcrops and boulders may experience little chemical weathering (e.g. Carson and Kirkby, 1972; Oberlander, 1972). Average hillslope P may provide a better estimate of the landscape erosion rate because it is more sensitive to precipitation and boundary condition.

Soils on non-eroding alluvial surfaces show extreme sensitivity to MAP in their salt composition and concentration (Ewing *et al*., 2006), in the degree of chemical weathering (Ewing *et al*., 2006; Amundson *et al*., 2007), and in the abundance of microbial life (Navarro-González *et al*., 2003; Warren-Rhodes *et al*., 2006). Gypsum, anhydrite, halite, carbonate, iodate and borate are found in alluvial soils in the northern part of the Atacama, above ~24°S (Ericksen, 1981; Ewing *et al*., 2006), due in part to the deposition of material derived from marine and volcanic sources in the region (Böhlke *et al*., 1997; Rech *et al*., 2003; Michalski *et al*., 2004). As precipitation increases, the salt content of alluvial soils decreases and organic matter increases (Ewing *et al*., 2006).

Uplift of the Coastal Cordillera between 22°–33°S has averaged 0·2 mm a^{-1} over the last 100–800 ka (Figure 2d). Long profiles of rivers cutting through the Coastal Cordillera at these latitudes have convex or straight regions near the coast, indicative of a geomorphic system out of equilibrium with baselevel (Mortimer, 1980). Hypsometric curves (the cumulative fraction of total area versus normalized elevation) of the land surface of the Atacama Desert are generally convex (Montgomery *et al*., 2001), a pattern consistent with a landscape where fluvial incision is unable to match tectonic uplift. This suggests that inland hillslopes are isolated from current marine baselevel and local channel incision may differ greatly from uplift rate.

Methods

Site selection

Pairs of non-landsliding, convex, granitic hillslopes were selected in three climate regions: hyperarid, arid, and semi-arid (Figure 2, Table I), all of which receive precipitation from the west. In each pair, one hillslope is bounded by an actively incising channel (currently bedrock-bedded) and the other is bounded by a stable landform (e.g. uppermost stream terrace, pediment, or alluvial fan) (Figures 2 and 3). These are referred to as the 'active hillslope' and 'stable hillslope', respectively. This nomenclature is not meant to imply that the stable hillslope is not eroding, only that its boundary is currently inactive and isolates the hillslope from regional baselevel conditions.

The precipitation gradient spans two-orders of magnitude (Figure 2b, Table I), with MAP decreasing from 119 mm, to 9·5 mm, to <2 mm for the semi-arid, arid, and hyperarid regions, respectively (McKay *et al*., 2003; Worldclimate.com, accessed November 18, 2009). The range of MAP is one- to two-orders of magnitude within each region. MAP is likely not the best metric for geomorphically important precipitation because in arid regions erosion is often driven by large, rare events (e.g. Coppus and Imeson, 2002, and references cited therein). However, it is the only precipitation metric available in this little-studied area.

Fog input also varies between sites due to their varying elevations and distance inland from the coast (Table I). This variation was unavoidable because analysis of ^{26}Al and ^{10}Be requires quartz, and quartz-bearing rock is relatively rare in the southern part of our study. Dew and fog contribute another 5–10 mm a^{-1} of moisture in the semi-arid region (Kalthoff *et al*., 2006). Fog inputs at the arid site are frequent due to the local connection to the coast via an east-west trending valley, and great enough to support scattered fog-adapted vegetation, but unquantified. Fog input is modest in the hyperarid region due to the elevation and distance inland (Cáceres *et al*., 2007). Because fog inputs enhance the precipitation gradient, they do not compromise the interpretation of our results. MAT decreases slightly from north to south (Table I), but this difference is less than one-order of magnitude. Thus, the largest climate signal is precipitation.

Field observations and analyses

On each hillslope,10–40 soil pits were excavated, 5–6 of which formed a slope-parallel transect extending from the ridge top (or as close to the ridge top as possible) to the bottom of the hillslope (Figure 4). Soil thickness was measured in all

Table I. Comparison of hillslope characteristics

	Semi-arid	Arid	Hyperarid
MAP (mm) (average, range)[a]	119, 10–410	9·5, 0–80	<2, 0–?
MAT (°C) (average, range)[b]	13·5, 21–8	16, 27–11	17, 32–0
Elevation (masl)	400	680	1170
Distance from coast (km)	15	21	50
Plant density (% area)	32	6	0
Bedrock[c]	Pluton Santa Gracia: 100 Ma, felsic, coarse-grained monzogranite	Pluton Cerros del Vetado: 217 Ma, coarse-grained monzogranite (contains mafic dikes but none were in the studied hillslopes)	Unidad Herradura: middle-Cretaceous, mafic, fine-grained granodiorite
Incision rate of active boundary (m Ma^{-1})[d]	34 ± 1·7	3·7 ± 0·1	0·9 ± 0·5
Age of stable boundary surface (Ma)	0·25 ± 0·11	0·63 ± 0·14[e]	Pliocene-Holocene
Average slope-normal soil thickness (cm) (active/stable)	14·6 ± 6·7 / 23·2 ± 6·4	2·0 ± 3·4 / 4·6 ± 4·6	5·5 ± 3·5 / 76 ± 22
Average bedrock erosion rate (m Ma^{-1}) (active/stable)[d]	26 ± 7·0 / 11 ± 2·7	2·7 ± 0·4 / 0·75 ± 0·70	0·96 ± 0·31 / 0·62 ± 0·94
Geomorphic processes	Bioturbation, chemical weathering	Bioturbation, salt shrink–swell, overland flow	Salt shrink–swell, overland flow

[a] Semi-arid MAP is an 80-year average for La Serena from Worldclimate.com (accessed November 18, 2009) and the range is from Kalthoff *et al*. (2006). Arid MAP is a 53-year average for Chañaral from Worldclimate.com and the range is from Rundel *et al*. (1996). Hyperarid data is from McKay *et al*. (2003) and is in general agreement with the Worldclimate.com data for Antofagasta, the nearest town.
[b] MAT data from Squeo *et al*. (2006), Rundel *et al*. (1996), and McKay *et al*. (2003), for the semi-arid, arid, and hyperarid sites, respectively.
[c] Geologic data from Emparan and Pineda (2000), Godoy and Lara (1998), and Marinovic *et al*. (1992) for the semi-arid, arid, and hyperarid sites, respectively.
[d] Incision rate and bedrock erosion rates were calculated using Equation 5 and are the average of the ^{10}Be- and ^{26}Al-derived values, except for the bedrock erosion rates of the arid stable hillslope which were calculated with Equation 7 and the incision rate of the hyperarid region which has been recalculated as described in the text.
[e] Arid stable boundary condition is given as the erosion rate of the pediplain adjacent to the stable hillslope (in m Ma^{-1}).

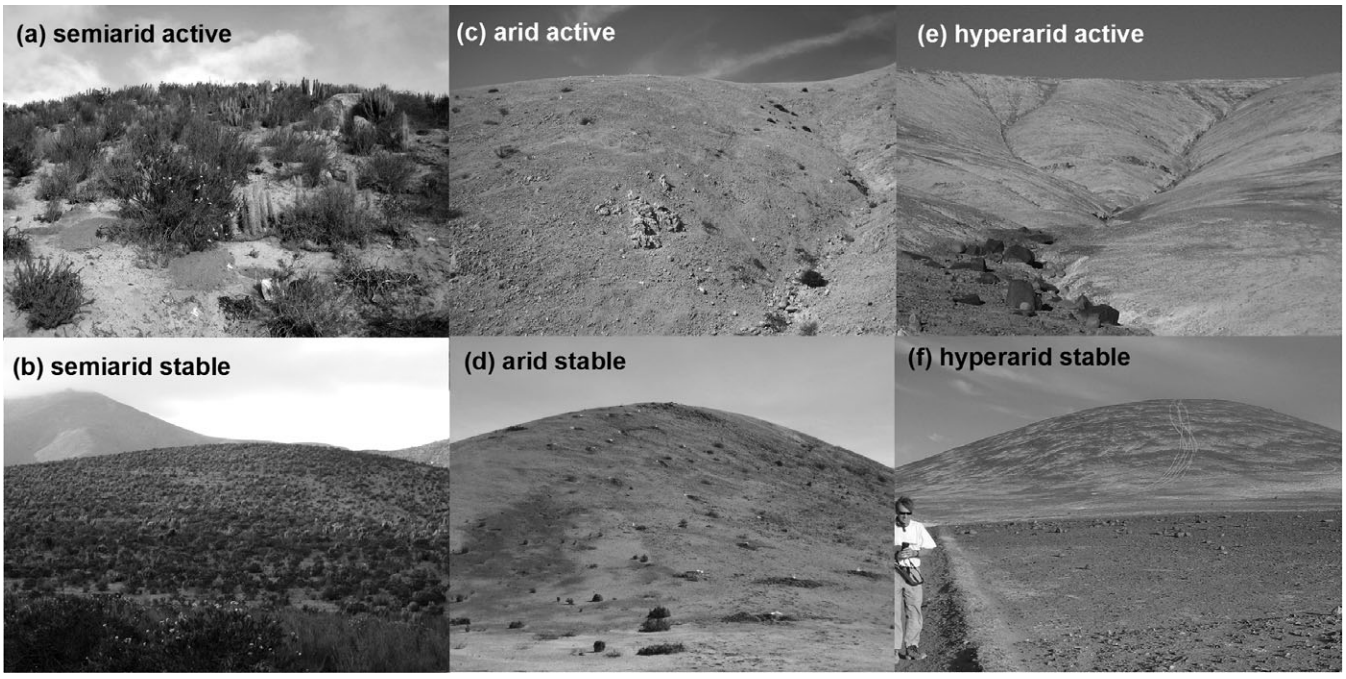

Figure 3. A pair of hillslopes with contrasting boundary conditions (actively incising channel versus non-eroding landform) was studied within each climate zone (semi-arid, arid, and hyperarid). (a) The semi-arid active hillslope, looking up-transect from the channel. (b) The semi-arid stable hillslope viewed from the bounding terrace. The arid active (c) and stable (d) hillslopes, looking uptransect. The hyperarid active (e) and stable (f) hillslopes, looking up-transect.

excavations, with the base of the soil defined as the transition to unexpanded or unperturbed bedrock textures at the semi-arid and arid sites, and as the transition to >85% rock fragments at the hyperarid sites. The soils along the downslope transect were described for color, organic matter content, structure, porosity, and consistence following the methods of Schoenenberger *et al*. (2002) and were sampled by horizon for analysis of chemical composition, bulk density, and texture.

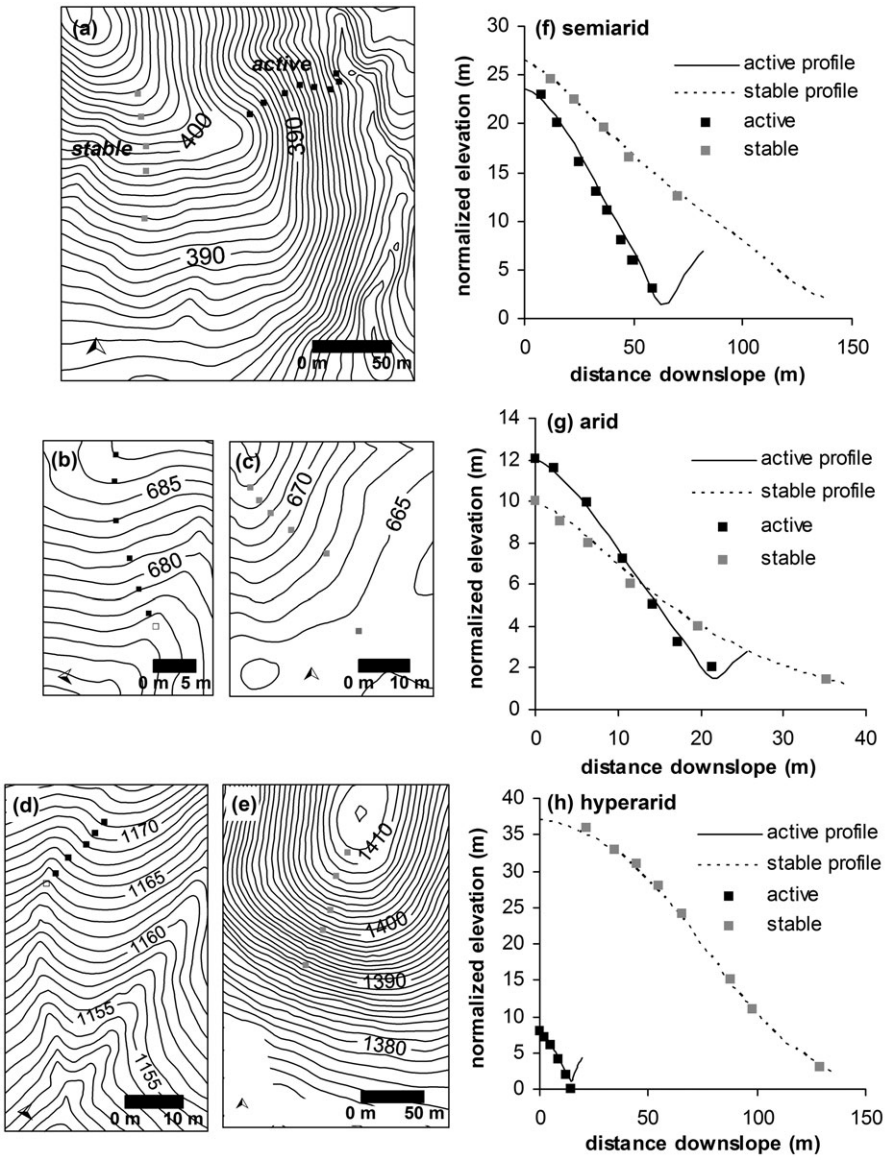

Figure 4. Topographic maps of the semi-arid (a), arid active (b), arid stable (c), hyperarid active (d), and hyperarid stable (e) hillslopes showing the locations of the sampled soil excavations. Each map has a different scale, but the contour interval is always 1 m. The differences in local relief, hillslope length, and slope between the hillslopes are clearer in elevation profiles of the semi-arid (f), arid (g), and hyperarid (h) hillslopes. Squares mark the sampled excavations. The elevations in (f), (g), and (h) were normalized by subtracting the elevation of the boundary condition (i.e. channel or terrace) from the actual surface elevation.

Evidence of the processes forming and transporting soil was recorded. Topographic surveys of each hillslope were made using a Trimble global positioning system (GPS) and analyzed with Golden Surfer Software (v. 8.0). Vegetation density was measured by calculating the length fraction underlain by vegetation along three 50-m transects on each hillslope.

Saprolite at the soil–saprolite interface (at the semi-arid sites) or fractured bedrock at the soil–bedrock interface (at the arid and hyperarid sites) was collected from excavations along the downslope transects for CRN analysis. On the semi-arid active hillslope, three additional saprolite samples near the transect were collected (Table II). Exposed bedrock from channels adjacent to the active hillslopes was collected to measure local incision rate. Quartz pebbles on the surface of the terrace bounding the semi-arid hillslope were collected and processed as an amalgamated sample to determine the exposure age of the stable boundary. Weathered bedrock from excavations in the pediplain surrounding the arid hillslopes was collected to determine the rate and uniformity of pediplain lowering.

The samples for CRN analysis were processed following Kohl and Nishiizumi (1992). The samples were ground to <0·5 mm. Quartz grains were isolated through a series of acid leaches, dissolved with HF-HNO_3 solution, and mixed with Be carrier. The concentration of Al in the quartz was measured by atomic absorption spectrometry, then Be and Al were chemically isolated and purified. $^{10}Be/^{9}Be$ and $^{26}Al/^{27}Al$ were measured by accelerator mass spectrometry (AMS) at the Lawrence Livermore National Laboratory Center for AMS and the Purdue Rare Isotope Measurement Laboratory and normalized to the ^{10}Be AMS standard (Nishiizumi *et al.*, 2007) or the ^{26}Al AMS standard (Nishiizumi, 2003), respectively. Accordingly, the ^{10}Be half-life of 1·36 Ma and the ^{26}Al half-life of 0·705 Ma were used. Erosion rates and exposure ages were calculated using the scaling functions of Lal (1991) and assuming 2·5% muon contribution at sea level. Production rates (at sea level and high latitude) of 5·1 atoms ^{10}Be g-quartz^{-1} a^{-1} and 34·1 atoms ^{26}Al g-quartz^{-1} a^{-1} were used after being corrected for modern soil cover thickness and bulk density. We report P calculated using both Equations 5 and 7, though Equation 7 could not be used for all samples.

Rock samples from the bedrock-soil interface were thin-sectioned by Spectrum Petrographics, Inc. (Vancouver, WA) and the Department of Earth and Planetary Sciences at the University of California, Berkeley (EPS-UCB). Samples from the hyperarid and arid sites were impregnated with epoxy and then cut using a waterless technique to preserve any salt within the rock fragments. The samples were imaged on a Leo 430 scanning electron microscope-energy dispersive X-ray spectrometer (SEM-EDS) at the EPS-UCB.

Table II. Topographic data, CRN measurements, and erosion rate calculation

Sample ID	Sample type	Distance downslope (m)	CRN sample depth (cm)	Slope- normal soil thickness (cm)	Soil bulk density (g cm^{-3})	Slope	^{10}Be[a] (atom g^{-1})	+/–[a]	^{26}Al[a] (atom g^{-1})	+/–[a]	^{26}Al/^{10}Be	+/–	From Equation 5[b]				From Equation 7[b,c]	
													^{10}Be minimum erosion rate (m Ma^{-1})	^{26}Al minimum erosion rate (m Ma^{-1})	Average erosion rate (m Ma^{-1})	+/–	^{26}Al/^{10}Be-derived erosion rate	+/–
Hyperarid active (24·13°S, 69·99°W, 1170 m.a.s.l.)																		
YH-05-16c	Hillslope bedrock	0	4·5	4·2	0·80	0·40	2·61E+06	1·19E+05	1·41E+07	7·47E+05	5·39	0·38	0·95	0·95	0·95	0·05	0·93	0·49
YH-17-4	Hillslope bedrock	2·5	5	4·7	0·81	0·34	2·89E+06	3·55E+04	1·50E+07	4·34E+05	5·19	0·16	0·83	0·85	0·84	0·02	0·72	0·15
YH-18-4	Hillslope bedrock	5·0	24	21·6	0·81	0·49	2·70E+06	4·64E+04	1·39E+07	4·39E+05	5·15	0·19	0·91	0·97	0·94	0·04	0·69	0·16
YH-19-C	Hillslope bedrock	8·8	9	7·6	0·60	0·62	2·61E+06	3·27E+04	1·47E+07	5·17E+05	5·64	0·21	0·95	0·88	0·91	0·05	1·3	0·4
YH-20-C	Hillslope bedrock	12·2	7	5·9	0·79	0·65	2·32E+06	3·90E+04	1·22E+07	3·59E+05	5·27	0·18	1·1	1·2	1·2	0·1	0·79	0·18
YH-05-44b	Channel bedrock	14·6	0	0	NA	NA	2·03E+06	5·03E+04	8·34E+06	5·07E+05	4·11	0·27	1·3	2·1	1·7	0·5	0·15	0·08
Hyperarid stable (24·38°S, 69·94°W, 1450 m.a.s.l.)																		
ORH-06-4	Hillslope bedrock	21·6	36	35·6	2·17	0·14	5·36E+06	9·27E+04	2·64E+07	1·26E+06	4·92	0·25	0·29	0·20	0·25	0·06	0·52	0·17
ORH-06-3	Hillslope bedrock	34·9	57	56·5	2·32	0·13	5·67E+06	2·40E+05	2·98E+07	3·69E+06	5·27	0·69	0·10	0·18	0·11	0·26	0·80	0·91
ORH-06-13	Hillslope bedrock	44·9	70	68·2	1·04	0·23	4·61E+06	1·89E+05	1·86E+07	1·66E+06	4·03	0·40	0·39	0·56	0·48	0·12	0·13	0·12
ORH-2-4	Hillslope bedrock	54·7	9	8·7	0·55	0·27	3·39E+06	3·88E+04	1·05E+07	4·56E+05	3·10	0·14	0·66	1·5	1·1	0·6		
ORH-06-18	Hillslope bedrock	65·6	75	71·7	0·55	0·31	5·00E+06	1·75E+05	1·88E+07	2·13E+06	3·76	0·45	0·34	0·55	0·44	0·15	0·06	0·11
ORH-1-5	Hillslope bedrock	87·7	57	53·6	1·08	0·36	4·47E+06	1·04E+05	7·11E+06	5·84E+05	1·59	0·14	0·42	2·5	1·5	1·5		
ORH-06DC9	Hillslope bedrock	98·3	85	~81	1·24	NA	6·10E+06	1·50E+05	2·74E+07	9·75E+05	3·20	0·40	0·32	0·72	0·52	0·28		
ORH-05-RC	Hillslope bedrock	129·2	80	~76	1·22	NA	4·60E+06	1·28E+05	1·95E+07	6·63E+05	4·50	0·19	0·22	0·17	0·19	0·03	0·29	0·08
Arid active (26·28°S, 70·49°W, 687 m.a.s.l.)																		
CH-1	Hillslope bedrock	0	2·5	2·4	1·32	0·21	1·10E+06	2·61E+04	6·15E+06	2·39E+05	5·57	0·25	2·7	3·0	2·9	0·2	1·2	0·4
CH-2	Hillslope bedrock	2·3	2	1·9	1·20	0·40	1·06E+06	2·50E+04	5·93E+06	2·77E+05	5·61	0·29	2·9	3·1	3·0	0·2	1·2	0·5
CH-3	Hillslope bedrock	6·3	2	1·8	1·15	0·51	1·06E+06	2·53E+04	5·95E+06	2·12E+05	5·63	0·24	2·9	3·1	3·0	0·2	1·3	0·5
CH-4	Hillslope bedrock	10·7	4	3·6	1·16	0·51	1·21E+06	3·48E+04	6·99E+06	3·97E+05	5·76	0·37	2·4	2·6	2·5	0·1	1·6	1·0
CH-5	Hillslope bedrock	14·3	2	1·7	1·07	0·67	1·27E+06	3·58E+04	7·03E+06	2·45E+05	5·53	0·25	2·3	2·6	2·4	0·2	1·1	0·4
CH-6	Hillslope bedrock	17·3	3·5	3·1	1·42	0·53	1·23E+06	5·65E+04	7·18E+06	3·63E+05	5·85	0·40	2·4	2·5	2·4	0·1	1·8	1·5
CH-7	Channel bedrock	19·1	0	0	NA	NA	8·53E+05	2·16E+04	5·12E+06	2·62E+05	6·00	0·34	3·6	3·8	3·7	0·1	2·3	1·9
Arid stable (26·28°S, 70·49°W, 670 m.a.s.l.)																		
CHS-1	Hillslope bedrock	0	2	1·9	1·96	0·27	1·55E+06	3·51E+04	8·36E+06	3·47E+05	5·39	0·26	1·8	2·0	1·9	0·1	0·94	0·32
CHS-2	Hillslope bedrock	3·1	3·5	3·3	1·26	0·36	1·54E+06	3·58E+04	7·52E+06	2·23E+05	4·88	0·18	1·9	2·3	2·1	0·3	0·49	0·12
CHS-3	Hillslope bedrock	6·4	2·5	2·4	1·19	0·31	1·56E+06	3·81E+04	9·17E+06	2·74E+05	5·89	0·23	1·8	1·8	1·8	0·0	1·9	0·8
CHS-4	Hillslope bedrock	11·6	3	2·8	1·19	0·36	2·33E+06	4·54E+04	1·04E+07	3·36E+05	4·45	0·17	1·1	1·5	1·3	0·3	0·27	0·07
CHS-5	Hillslope bedrock	19·8	4	3·9	1·06	0·25	2·38E+06	6·67E+04	1·21E+07	3·56E+05	5·06	0·21	1·1	1·2	1·1	0·1	0·61	0·16
CHS-06-7	Low erosion surface	35·3	11	10·9	1·5	0·11	3·89E+06	6·61E+04	1·64E+07	8·24E+05	4·21	0·22	0·53	0·73	0·63	0·14	0·18	0·08
CHA-PP	Pediplain channel	NA	11	~11	~1·5	~0	1·68E+06	6·80E+04	5·54E+06	3·40E+05	3·30	0·24	1·7	3·4	2·5	1·2		
CHS-PP	Pediplain interfluve	NA	44	~44	~1·5	~0	2·94E+06	8·80E+04	1·54E+07	8·20E+05	5·25	0·32	0·81	0·81	0·81	0·03	0·77	0·33
Semiarid active (29·77°S, 71·08°W, 377 m.a.s.l.)																		
SGA-1	Hillslope saprolite	7·7	7	6·7	1·35	0·29	2·42E+05	5·81E+03	1·98E+06	1·62E+05	8·21	0·70	23	18	20	1·7		
SGA-2	Hillslope saprolite	15·4	10	9·4	1·70	0·36	1·58E+05	4·42E+03	1·15E+06	7·15E+04	7·25	0·50	35	32	33	2·3		
SGA-3	Hillslope saprolite	25·4	15	13·8	1·50	0·42	1·74E+05	4·85E+03	9·74E+05	6·46E+04	5·61	0·40	32	37	35	2·7	2·1	1·3
SGA-4	Hillslope saprolite	33·2	14	13·0	1·40	0·40	1·52E+05	4·14E+03	1·08E+06	5·09E+04	7·08	0·39	36	34	35	1·9		
SGA-06-28	Hillslope saprolite	38·2	22	20·3	1·50	0·41	2·26E+05	1·15E+04	1·14E+06	8·89E+04	5·04	0·47	24	32	28	5·3	1·0	0·6
SGA-06-17	Hillslope saprolite	44·4	17	15·9	1·51	0·38	2·63E+05	1·84E+04	1·56E+06	1·03E+05	5·95	0·57	21	23	22	1·5	3·5	8·3
SGA-06-16	Hillslope saprolite	49·6	24	22·2	1·49	0·41	3·25E+05	1·83E+04	2·03E+06	1·38E+05	6·25	0·55	17	17	17	0·8		
SGA-5	Hillslope saprolite	50·2	30	27·0	1·38	0·48	3·09E+05	8·06E+03	2·11E+06	1·93E+05	6·84	0·65	18	17	17	1·7		
SGA05-14b	Channel bedrock	59·2	0	0	NA	NA	1·02E+05	7·24E+03	6·33E+05	4·18E+04	6·24	0·61	33	35	34	1·7		
Semiarid stable (29·78°S, 71·08°W, 400 m.a.s.l.)																		
SGS-1	Hillslope saprolite	12	37	36·6	1·43	0·15	4·10E+05	1·03E+04	2·60E+06	2·13E+05	6·33	0·54	13	13	13	1·2		
SGS-2	Hillslope saprolite	22·9	15	14·7	1·49	0·21	4·88E+05	1·42E+04	3·40E+06	2·26E+05	6·98	0·50	11	9·9	10	0·8		
SGS-3	Hillslope saprolite	36·8	22	21·4	1·38	0·23	6·54E+05	2·39E+04	3·19E+06	2·13E+05	4·88	0·41	8·0	11	9·3	1·9	0·82	0·45
SGS-22b	Hillslope saprolite	48·3	25	24·6	1·46	0·18	5·71E+05	1·53E+04	3·17E+06	1·98E+05	5·56	0·38	9·3	11	10	1·0	2·0	1·1
SGS-21	Hillslope saprolite	70·5	25	24·6	1·46	0·18	5·55E+05	1·39E+04	3·38E+06	2·77E+05	6·09	0·52	9·6	10	9·8	0·3	4·5	18·1
SGS-Q	Non-eroding surface	>100	0	0	NA	0·09	1·42E+06	2·97E+04	4·66E+06	2·08E+05	3·29	0·16	300[d]	147[d]	224[d]	108[d]		

[a] ^{10}Be and ^{26}Al concentrations are reported as normalized to sea level and high latitude using the scaling factors of Lal (1991). Uncertainty values are 1 – σ uncertainty in the AMS analysis and do not include the uncertainty of the production rates or half lives of the CRN.
[b] Erosion rates were calculated using latitude and altitude-corrected CRN concentrations, and assuming rock density = 2·5 g cm^{-3} and saprolite density = 1·5 g cm^{-3}.
[c] Negative erosion rates are not reported (blank squares).
[d] For SGS-Q, the values are minimum exposure ages (in ka), rather than erosion rates.
NA = not available.

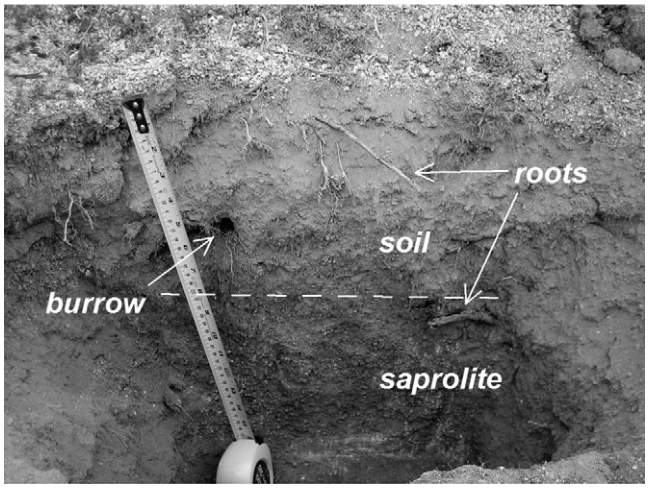

Figure 5. A soil profile on the semi-arid active hillslope. Bioturbation is apparent in roots, root traces, and burrows extending to the soil–saprolite boundary, which are the main processes converting the saprolite into soil. The dashed white line marks the approximate boundary between the soil and saprolite. Note that the saprolite is not considered part of the soil because it has not been physically transported.

Results

Both boundary condition and MAP exert control on landscape development. In order to tease apart their contributions, the results from each climate region are presented separately before a site-to-site comparison is made. For each site we describe the soils, identify the processes of soil formation and transport, and quantify the rate of soil production.

Semi-arid hillslopes

The semi-arid hillslopes provide useful reference points because the climate is wet enough to support vegetation and animals as well as drive chemical weathering. Thus, the soil production and transport processes are similar to those found in previous studies of semi-arid to humid hillslopes (e.g. Heimsath *et al*., 1999; Yoo *et al*., 2005). The availability of water, CO_2, and organic matter in the soil facilitates deep weathering, and hand excavations could not reach unweathered bedrock. Thick, red, clay films surround in-place mineral grains in the saprolite and weathered bedrock. Carbonate and other salts were undetectable in the soils. The soil surface is coarse sand and fine gravel which overlie a dense, finer-textured soil interwoven with roots. Cacti and shrubs cover 32% of the soil surface (Figures 2a and 2b) and their roots, though concentrated in the upper tens of centimeters of the soil, extend into the top of the saprolite (Figure 5). The vegetation is patchy, leaving areas of bare ground, but the coarse-textured surface limits rainsplash and minimizes overland flow, except for strongly disturbed areas where trails have been eroded tens of centimeters deep. The vegetation supports small burrowing mammals and insects, as well as introduced grazers (including mules, horses, and goats). A population of native grazers likely existed prior to ranching (Wheeler, 1995). Chemical weathering (as evidenced by clay films and soil reddening) weakens the bedrock and leads to some chemical erosion, while bioturbation (as evidenced by burrows and root traces) disrupts the weathered bedrock, converts it to soil, and transports it downslope. Wetting and drying of the soil likely produces some shrink–swell driven soil creep (Kirkby, 1967). Bioturbation and soil creep are depth dependent (e.g. Kirkby, 1967; Gabet *et al*., 2003; Yoo *et al*., 2005) and slope dependent (Heimsath *et al*., 1999; Braun *et al*., 2001; Yoo *et al*., 2007). Thus, hillslopes with different boundary conditions in this region should have different values of P and H.

The active hillslope is bounded by a small tributary of the Quebrada de Santa Gracia and Rio Elqui (the major drainage from the Andes at this latitude), draining to La Serena Bay (~20 km downstream). The Quebrada de Santa Gracia is a gravel-bedded, braided river that rarely flows [the last major flood was in 1997 during a strong El Niño year (Pérez, 2005)]. Sediment records from the bay show that this region, like most of the Chilean coast, experienced periods of uplift and transgression during the Miocene (Le Roux *et al*., 2006). Over the last 2·1 Ma, the coast has uplifted ~80 m Ma^{-1} relative to sea level (Le Roux *et al*., 2005). The channel adjacent to the active hillslope has an incision rate of 34 $\pm$ 2 m Ma^{-1} (sample SGA05-14b, Tables I and II, we use Equation 5 because the CRN concentrations are low), less than half of the average Quaternary uplift rate. The sample plots near the steady-state erosion line in $^{26}Al/^{10}Be$—^{10}Be space (Figure 6a), indicating that the calculated P represents the average over the last 20 ka. The difference between the incision rate at the base of the active hillslope and the regional uplift rate suggests that signal of marine baselevel has not been fully transmitted upstream.

The stable hillslope is located on the other side of the ridge and is bounded by the highest of a series of stream terraces along the Quebrada de Santa Gracia (Figures 3b and 4a). The terrace gravel sample had a minimum exposure age of 220 $\pm$ 110 ka (Equation 8). The $^{26}Al/^{10}Be$ ratio of this sample is low (Figure 6a) indicating a complex exposure history. This is not unexpected because the sampled gravels were small and have probably moved for longer than 220 ka. Additionally, bioturbation could have buried and brought to the surface some of the pebbles. The CRN calculation gives a minimum apparent exposure time, so it is likely that the uppermost terrace formed at least 220 ka.

Active hillslope H values increase downslope from 7 to 27 cm, with an average of 14·5 $\pm$ 6·7 cm (n = 30) (Figure 6b). Deviations from constant H are sometimes interpreted as evidence of deviation from steady state, but this applies only if soil flux is solely dependent on slope. Other expressions of soil flux produce non-uniform H on steady-state hillslopes (e.g. Furbish, 2003), and are expected for many biotic hillslopes (Heimsath *et al*., 2005). Stable hillslope H are higher than on the active hillslope, averaging 23·2 $\pm$ 6·4 cm (n = 25). They increase slightly downslope (Figure 6b), but were expected to increase more given the stable boundary condition. The absence of soil accumulation at the base may be due to the uniformly low gradient across the hillslope (averaging 0·19 $\pm$ 0·03 versus 0·39 $\pm$ 0·06 on the active hillslope, Figure 4f) and its location upslope from the concave transition from hillslope to terrace (>60 m, Figure 4a).

Most data points from both hillslopes plot near the steady-state erosion window in Figure 6(a), within $\pm 2\sigma$ error ($\pm 1\sigma$ error is plotted in Figure 6a). Thus, they suggest that H and P have been nearly constant, at least for the last ~10^4 a. The P calculated from both Equations 5 and 7 are reported where possible (Table II), but the relatively low CRN concentrations ($^{26}Al/^{10}Be$ ratios near R_0) result in erroneous P values using Equation 7. These values are negative (and therefore impossible) or incongruously low (based on the evidence of extensive bioturbation and disruption of the soil–bedrock interface). Thus, we focus on P calculated from Equation 5.

Average P is greater on the active hillslope than the stable hillslope (26 $\pm$ 7 m Ma^{-1} versus 11 $\pm$ 3 m Ma^{-1}, respectively) (Table I). When considered with the difference in average hill-

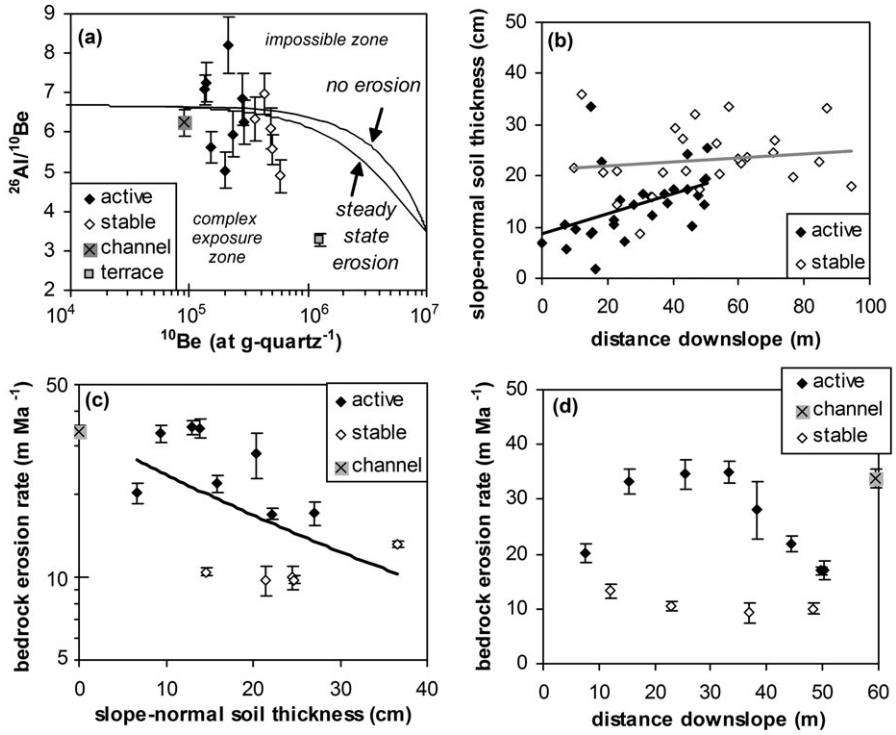

Figure 6. Semi-arid hillslope data. Error bars are 1σ uncertainty in the AMS analysis. (a) Most cosmogenic radionuclide data from both the active and stable hillslope plot near the erosion window and indicate near steady-state bedrock erosion and soil cover for ~20 ka. Data plotting below the erosion window indicate samples have experienced a complex exposure history including changes in the overlying soil thickness or the bedrock erosion rate. The sample from the terrace adjacent to the stable hillslope is an amalgamated sample of several gravels, which have experienced a complex exposure history. (b) Slope-normal soil thickness increases with distance downslope on the active hillslope but is essentially constant on the stable hillslope. Soil thickness is greater on the stable hillslope than active hillslope. (c) The rate of soil production from bedrock on the semi-arid hillslopes is correlated to slope-normal soil thickness. If all data points are considered $P = 34{\cdot}2e^{-0{\cdot}0337H}$ ($r^2 = 0{\cdot}30$). (d) The rate of soil production from bedrock varies parabolically with distance downslope on the active hillslope but is nearly constant on the stable hillslope.

slope H, these data suggest that the boundary condition affects bedrock erosion in this region through the slope-thickness-erosion feedbacks described earlier. Indeed, P appears to decrease exponentially with increasing soil thickness, with $P = 34{\cdot}2e^{-0{\cdot}0337H}$ ($r^2 = 0{\cdot}30$) when data from both hillslopes are considered (H is in centimeters as in Heimsath *et al.*, 1997) (Figure 6c).

Based on the trends in Figures 6(b) and 6(c), P should monotonically increase with distance from the channel as H decreases. P is ~35 m Ma^{-1} at the channel and the excavations between 15–40 m downslope, and decreases to ~20 m Ma^{-1} at the lowest hillslope positions and at the uppermost excavation (SGA-1) (Figure 6d). Excluding SGA-1, the trend in P versus distance downslope varies as expected based on H. From 40 m downslope to the channel, the hillslope is slightly concave (average $\nabla^2 z = -0{\cdot}0064$ m^{-1}, Figure 4f). This hillslope form is inconsistent with steady channel incision, and, in combination with the lower P on this portion of the hillslope, suggests some transient variation in channel incision rate has been recorded across the hillslope.

SGA-1 has a low P relative to the other upslope positions on the active hillslope. The similarity in P between SGA-1 and SGS-1(the highest point on the stable hillslope) suggests that the midslope P (35 m Ma^{-1}) has not propagated all the way up the active hillslope. SGA-1 also has a low H compared to the rest of the active hillslope. This may be because a trail follows the ridge between the two transects (but favors the side towards the active slope) resulting in deep, slope-parallel rilling which has locally thinned the soil. Guanacos (coastal cameloids similar to llamas) create trails and have occupied the area for thousands of years (Wheeler, 1995), but these trails do not show the same degree of erosion based on our few observations. Temporary human settlements in this region of Chile are 12–13 ka (Mostny, 1972; Jackson *et al.*, 2007). An agricultural culture developed in the Elqui valley ~2 ka (Mostny, 1972) and the region has been inhabited ever since. If humans were responsible for the formation of the trail, then the removal of soil from the ridge is a geologically recent phenomenon and may not have yet affected erosion rates, depending on the response time of P to changes in H.

However, P on the stable hillslope is nearly constant except for the uppermost excavation which is higher (SGS-1, 13·2 ± 0·3 m Ma^{-1}) (Figure 6d). The consistency of H and P suggests that it may be in a relict steady state, adjusted to an incision rate of ~10 m Ma^{-1}, and the effect of the stable boundary has not propagated significantly upslope.

In summary, H and P on the active hillslope are thinner and faster, respectively, compared to the stable hillslope. These values may record the effect of variations in channel incision on the active hillslope, whereas they indicate the stable hillslope may be near steady state, but a steady state adjusted to a previous boundary condition.

Arid hillslopes

The arid hillslopes lie in the biotic-abiotic transition zone and have sparse soil cover (generally ≤3 cm) and biota (Figures 3c and 3d). The soil cover, where present, is dominated by coarse sand and fine gravels that abruptly overlie fractured bedrock (Figure 7a). Road cuts in the area reveal bedrock joint systems extending >6 m-deep (Figure 7b). The bedrock shows almost no evidence of chemical weathering (only a few reddish rinds are visible in thin section) and no saprolite. Accumulations of

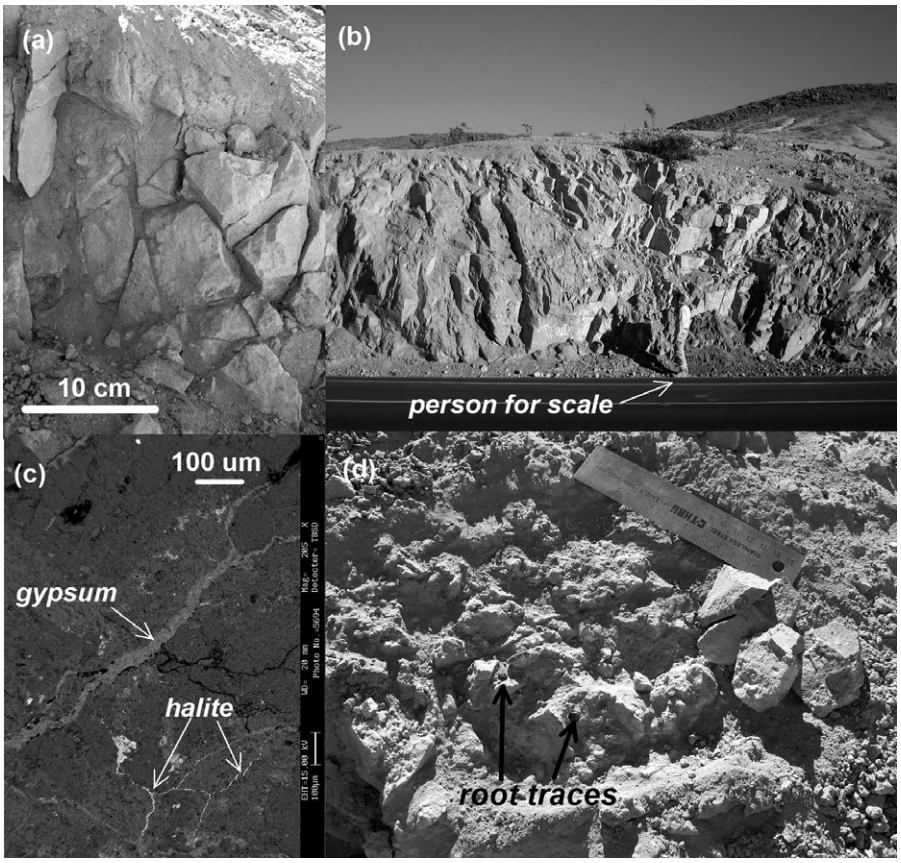

Figure 7. (a) An example of a soil profile at the arid site showing the thin, sandy soil underlain by fractured bedrock. (b) A nearby road cut showing the deep fracturing in the bedrock. (c) An SEM-EDS image showing salt accumulation in microcracks in the bedrock. (d) The exposed soil–bedrock interface showing the rounding of the tops of the bedrock fragments below the soil and root traces extending into the dust-filled cracks.

gypsum and halite in microfractures are detectable with SEM-EDS (Figure 7c). Vertical fractures in the near-surface bedrock are filled with fine, reddish-brown dust. The dust is loose in the fractures and does not form films on the rock fragments. Based on observations during a fog event, the dust may act as a wick, transporting fog water and salt into the bedrock. Bedrock fragments extend vertically into the soil, but unlike the fractures a few centimeters deeper, the upper ends of these fragments are rounded and slightly chemically altered (Figure 7d). This rounding may be due to granular disintegration by chemical and salt-driven physical weathering driven by fog condensation and salt deposition on the surface. But bioturbation may also contribute to rock fracturing.

Shrubs and cacti cover 6% of the ground surface (Figures 3b and 3c). Roots and root traces were found in dust-filled fractures across the hillslopes suggesting that over long timescales the bioturbative effect of vegetation is dispersed over the entire hillslope (Figure 7d). Guanaco paths crisscross the hills, and this trampling dislodges bedrock fragments and mobilizes them downslope. Although burrowing lizards and insects are present in the region, they are found only on the plains surrounding the hills and not on the hills themselves due to the shallow soil cover. Small-scale surface gravel sorting on the hillslopes (Figure 8) suggests that rare overland flow events may transport material. Indeed, despite the arid climate, soil transport appears to be through both bioturbation and overland flow and should be largely slope-dependent.

MAP was greater 2 Ma ago than at present, during which time the hillslopes were likely mantled with a chemically-weathered soil which overlay saprolite. The absence of any trace of this weathered material on the hillslopes today suggests that this material was eroded, possibly quite rapidly, during aridification. Similarly, the removal of saprolite during aridification has been invoked as the formation mechanism of granitic boulder slopes in the Mojave Desert (Oberlander, 1972). This change in the soil mantle may be recorded in the CRN concentrations of the bedrock; they may have $^{26}Al/^{10}Be$ ratios that reflect the long-term hillslope *P* and low CRN concentrations that reflect the depth of the sample prior to the stripping of the soil. However, the CRN concentrations may have adjusted to the new exposure conditions if erosion has been fast enough and exposure long enough since the soil was stripped.

Figure 8. Surface-gravel sorting on a hillslope in the arid region which is highlighted by the colonization of coarse gravels by dark-colored lichens.

The hillslopes are surrounded by an expansive pediplain grading to the Quebrada de Peralilla. About 1 km from the coast, the Peralilla drops over a cliff formed by a fault (Grocott and Taylor, 2002). The fault has created a knickpoint which has not propagated upchannel, isolating the study site from present-day sea level (similar to the hanging valleys of Wobus *et al.*, 2006). The pediplain is covered with a network of shallow (<1-m-deep) channels. Excavations in non-

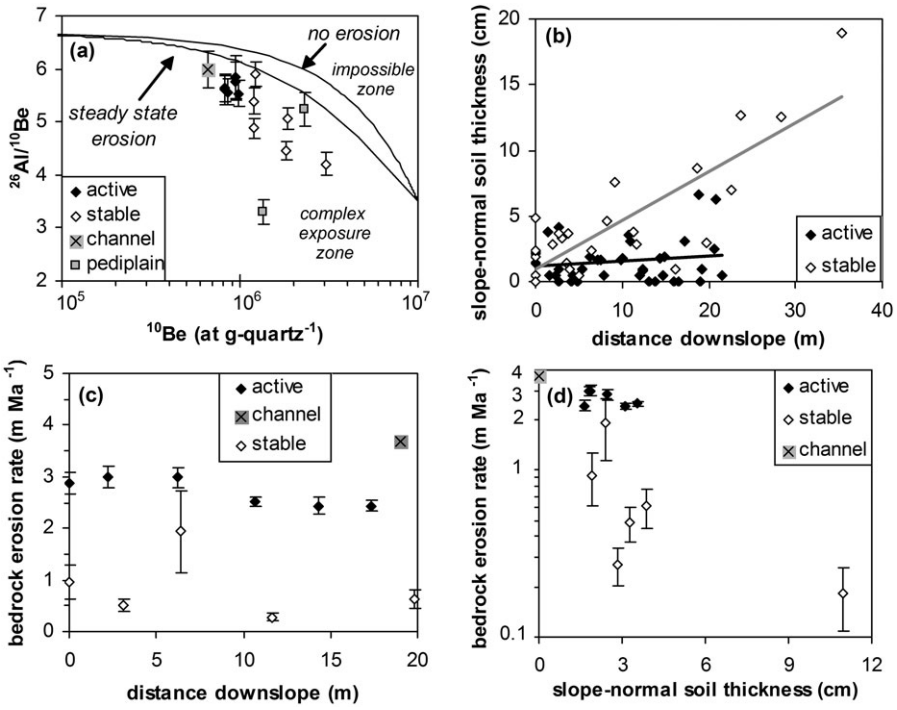

Figure 9. Arid hillslope data. Error bars are 1σ uncertainty in the AMS analysis. (a) Samples from the active hillslope and the channel are tightly clustered near the steady-state erosion line, whereas values from the stable hillslope and pediplain range from the steady-state erosion line to well below it. (b) Soil thickness is nearly constant with distance downslope on the active hillslope, whereas it increases on the stable hillslope. (c) The bedrock erosion rate is consistently higher on the active hillslope than the semi-arid hillslope, but varies little with distance downslope on either slope. (d) The range of soil thicknesses on the hillslopes is too small to determine if there is a relationship between soil thickness and bedrock erosion rate.

channelized portions of the pediplain and from the sides of the channels show ~1 m of soil and soft saprolite overlie weathered bedrock. A sample from the soil–saprolite boundary from one interfluve plots on the steady-state CRN line (CHS-PP) (Figure 9a) and P is ~0·8 m Ma^{-1} (regardless of calculation method). In contrast, a sample near the soil–saprolite boundary from the side of a shallow (~1 m) channel in the pediplain (CHA-PP) plots below the erosion window. Thus, P calculated with Equation 5 (2·5 m Ma^{-1}) is an overestimate, but the ^{26}Al/^{10}Be ratio is so low that Equation 7 produces a negative P. This combination of ^{10}Be concentration and low ^{26}Al/^{10}Be ratio is possible if the sample at CHA-PP was experiencing near-zero erosion and was only recently exposed by the channel (<10^5 ya, i.e. t short enough that CRN concentrations have not adjusted to new exposure conditions). If this interpretation is correct, then the low ^{26}Al/^{10}Be ratios in the channel record the long-term ratio of these nuclides while the individual nuclide concentrations are low due to the shielding by the now-absent soil mantle (removed by meandering channels). The P values derived from Equation 5 are 2–3 times larger than those derived from Equation 7 (Table II) and are not consistent with the likely exposure history of these samples.

Despite the erosion of the pediplain, hillslopes with differing boundary conditions were identified. The active hillslope is bounded by a bedrock channel (Figures 3c and 4b) with ^{26}Al and ^{10}Be concentrations indicating near steady-state erosion, within error (Figure 9a). Because this sample (CH-7) has a relatively low ^{10}Be concentration and is near the steady-state erosion line, we use Equation 5 to calculate an incision rate of 3·1 ± 0·1 m Ma^{-1}. The stable hillslope faces away from the Peralilla (upslope along the pediplain), and small channels split around the hillslope, leaving a non-eroding wedge at the base of the slope (Figures 3d and 4c). A sample from an excavation in this wedge (CHS-06-7) had the lowest ^{26}Al/^{10}Be ratio (4·21, Figure 9a) and P (Table II) of the hillslope samples. Compared to the surrounding pediplain, it appears that the stable hillslope is responding to a boundary condition whose rate of erosion has slowed. This will produce changes in H and P progressively upslope as if a non-eroding boundary condition was emplaced, but the changes will be smaller in magnitude (e.g. Fernandes and Dietrich, 1997).

The active hillslope is convexo-planar, whereas the stable hillslope is convexo-concave (Figure 4g). Correspondingly, average H is slightly smaller on the active hillslope (2 cm, n = 40) compared to the stable one (4·6 cm, n = 25). H is almost constant on the active hillslope and the convexo-planar section of the stable hillslope, but increases in the concave section of the stable hillslope (Figure 9b). Though H is small, the difference in trends between the two hillslopes is indicative of slope-dependent soil transport and boundary condition forcing.

^{26}Al/^{10}Be ratios on the active hillslope plot slightly below the erosion window in a tight cluster (Figure 9a) and have ^{10}Be concentrations low enough that P calculated with Equation 5 are likely more accurate than those from Equation 7. Using Equation 5, P decreases slightly from ~3 to ~2·5 m Ma^{-1} downslope (Table II, Figure 9c) and P derived from Equation 7 are 30–50% slower. The similarity between hillslope P and the incision rate of the bounding channel indicate this hillslope is near geomorphic steady state (uniform lowering) and adjusted to its boundary condition. If a soil mantle was stripped and enough material was removed to alter the CRN concentrations and ratios as described earlier, the surface would require 200–400 ka to reset to steady-state CRN values (the time required to remove ~70 cm, about one attenuation length, of rock if P = 1·4–3 m Ma^{-1} and assuming ρ_r = 2·5 g cm^{-3}). This provides a minimum estimate of when the soil may have been removed.

In contrast, most data from the stable hillslope plot in the complex exposure zone (Figure 9a), with lower ^{26}Al/^{10}Be ratios and higher ^{10}Be concentrations compared to the active hillslope. These correspond to lower P than the active hillslope, regardless of calculation method (0·2–1·9 m Ma^{-1} with Equation 7, 0·6–2·1 m Ma^{-1} with Equation 5, Table II, Figure 9c). This is consistent with the hypothesis that the CRN concentrations in the active hillslope bedrock are more likely to be near steady state, whereas on the stable hillslope they should be progressively deviating from steady state. However, the CRN concentrations of the samples from the stable hillslope may reflect more than simple slowing of erosion and accumulation of soil progressing upslope because of the regional stripping of weathered material. The ^{10}Be concentrations measured in most of the samples from the stable hillslope are a factor of two

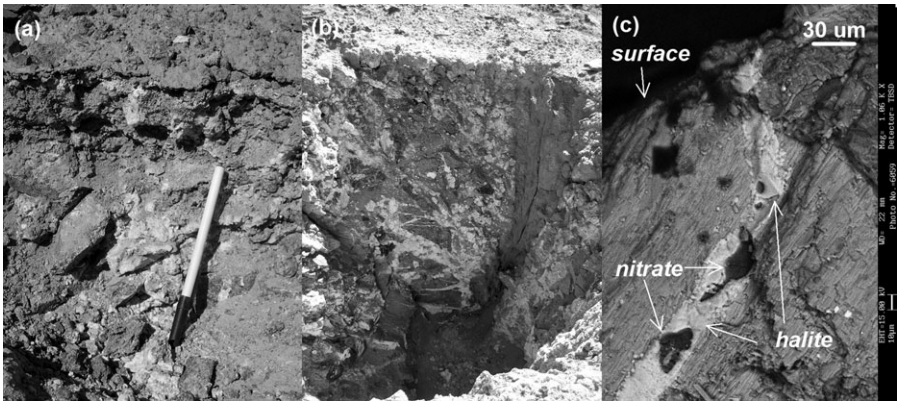

Figure 10. (a) A soil profile on the hyperarid active hillslope (pen is 15 cm long). (b) A soil profile near the summit of the hyperarid stable hillslope (excavation is 1 m deep). Angular, gray bedrock fragments are suspended in the white, gypsum-rich soil. The vertical feature on the right is a sandfilled crack. (c) SEM-EDS image of a rock fragment from the bedrock—soil interface on the active hillslope. The vertical crack is filled with both light gray halite and dark gray nitrate. The texture of the salt along the borders of the crack suggests episodes of dissolution and re-precipitation.

lower than the expected values from steady-state $^{26}Al/^{10}Be$ ratios. Many exposure histories can produce this combination of $^{26}Al/^{10}Be$ ratios and ^{10}Be concentrations, and without another cosmogenic nuclide we cannot definitively select one. However, one possible end member is steady, low erosion of 0·2–1·0 m Ma^{-1} for >1 Ma (to produce the low $^{26}Al/^{10}Be$ ratio), followed by recent ($\leq$ a few 10^5 a) removal of ~70 cm (~one-half an attenuation length if $\rho_s = 1{\cdot}5$ g cm^{-3}) of material above the samples. This is broadly consistent with our interpretation of the development of the soil in response to changing climate, described earlier. Though this model accounts for soil stripping during aridification, the extremely low *P* seem too low to represent rates under pre-aridification MAP (i.e. they are as much as three orders of magnitude smaller than the *P* calculated for the semi-arid site). The true *P* for samples with $^{26}Al/^{10}Be$ ratios in the complex exposure zone lie between those calculated from Equations 5 and 7. In any case, the active hillslope is near geomorphic steady state with a constant and relatively fast erosion rate, whereas the stable hillslope contains a record of non-steady erosion rates and/or soil thickness and is eroding slower. Though the differences in *P* and *H* between the two hillslopes might suggest some relationship between *P* and *H*, the range of *H* is too small to determine a trend (Figure 9d).

In summary, the active hillslope is near steady state and is eroding faster than the stable hillslope. Both have *P* and *H* significantly lower than the semi-arid hillslopes. The low $^{26}Al/^{10}Be$ ratios may record the stripping of the soil mantle less than a few 10^5 a ago, possibly in response to increasing aridity.

Hyperarid hillslopes

The soils on the hyperarid hillslopes are similar to soils on the adjacent alluvial fans in that they have accumulated atmospherically-deposited salts and are plant-free. Thus, hillslope processes are very different compared to the other sites. The soils on the hillslopes are a mixture of gypsum, nitrate, halite, and fine silicate dust, plus bedrock fragments ranging from sand to cobble size (Figures 10a and 10b). The bedrock fragments are angular and lack evidence of chemical weathering. Soils are comprised of a thin (~1–2 cm) surface layer of loose, fine-grained, silicate-rich material which is underlain by salt-rich, porous horizons with weak polygonal structure, which overlie increasingly salt-cemented, gravel-rich horizons (Figures 10a and 10b). Road cuts reveal deep (>4 m) fracture systems that are permeated with gypsum and halite. We considered the base of the horizon with polygonal structure development (above where rock fragment content >85%) as the relevant soil depth over geologic time, though on the stable hillslope the depth to this contact varied substantially (often >20 cm) over small distances. The polygonal soil structure is developed through the shrinking and swelling of soil salts, likely due to changes in soil moisture. On the stable hillslope, sand-filled cracks, tens of centimeters wide, penetrate to the soil–bedrock interface (Figure 10b). Though some cracking in northern Chile may be linked to earthquakes (Loveless *et al.*, 2005), shrink–swell events are the more likely cause because the material filling many of the cracks is layered, indicative of progressive crack opening and in-filling. The wetting events driving soil shrink–swell must be extremely rare, given the preservation of salts in the soils.

Biotic processes are essentially absent (Figures 3e and 3f). Instead, salt-driven processes and overland flow dominate erosion. Salt pries apart the rock using pre-existing fractures (Figure 10c) and eventually 'lifts' bedrock fragments into the soil column through salt growth and shrink–swell. Crystallization pressures of gypsum and halite have been modeled to be more than adequate to fracture rock (Winkler and Singer, 1972; Steiger, 2005), and many experimental studies support this (e.g. Rodriguez-Navarro and Doehne, 1999; Cardell *et al.*, 2003; Viles and Goudie, 2007). The polygonal soil structure indicates that salt shrink–swell is important in soil transport. Transport by clay shrink–swell is slope-dependent (e.g. Fleming and Johnson, 1975), and though no work has been done on salt-driven soil transport it is likely also slope-dependent. Sorting of surface gravels into contour-parallel bands (Figure 3f) suggests that overland flow occurs during extremely rare precipitation events. Thus, soil transport is likely slope-dependent but in a more complicated way than on the other hillslopes.

As at the other sites, the hillslopes in this region have experienced decreasing MAP, likely since the Miocene. Presently, the hillslopes are mantled with salt and dust which overlie fresh, fractured bedrock. Most hillslopes are surrounded by locally-derived alluvial fill. This alluvium was emplaced ~2·2 Ma based on ash and CRN dating (Ewing *et al.*, 2006). On a Pliocene alluvial fan near the active hillslope, root fragments were found at depth and provide evidence of semi-arid conditions prior to ~2 Ma (Ewing *et al.*, 2006). Thus, the slopes may have been mantled with weathered soil and saprolite (like the semi-arid site today) prior to 2·2 Ma. Decreased MAP led to the erosion of the soil and saprolite from the hillslopes (similar to the arid site today) to create the alluvium, an event that ended about 2·2 Ma. Since then, the previously exposed bedrock has been buried by eolian material and eroded by salt-driven mechanisms. As at the arid site, this variation in *P* and *H* may be recorded in bedrock CRN concentrations.

The active hillslope is located in an internally-drained basin which has been disconnected from marine baselevel since about the Pliocene. The incision rate of the channel bounding

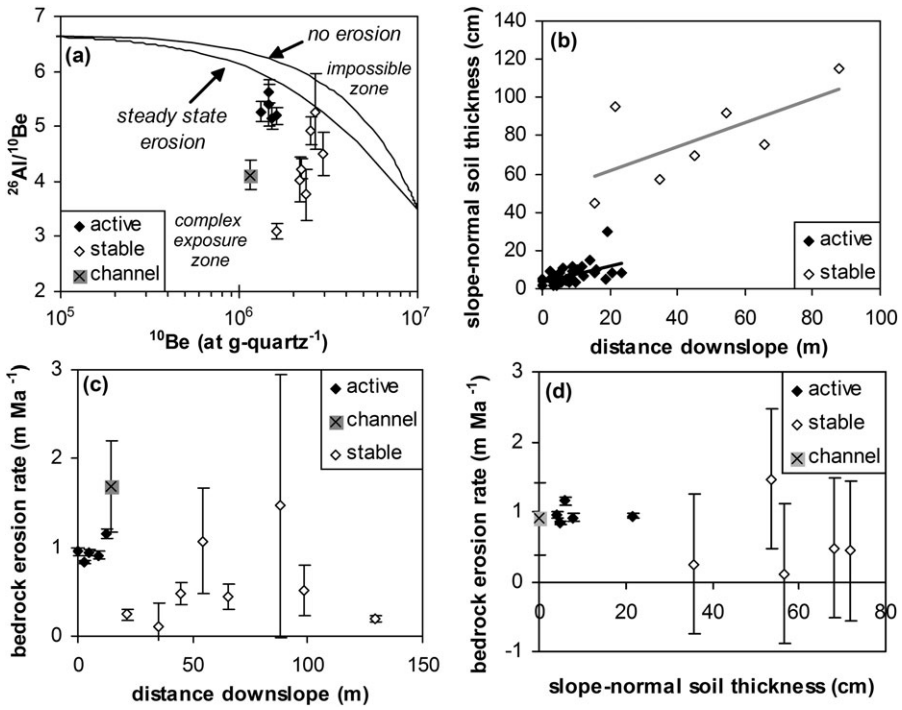

Figure 11. Hyperarid hillslope data. Error bars are 1σ uncertainty in the AMS analysis. (a) Soil thickness is constant on the active hillslope but increases with distance downslope on the stable hillslope. (b) The bedrock erosion rate (calculated with Equation 5) is nearly uniform with distance downslope on the active hillslope, showing a slight increase towards the channel, whereas they are consistently lower on the stable hillslope. (c) Samples from the active hillslope plot within the steady-state erosion window, whereas the channel sample plots in the complex exposure zone. As expected, samples from the stable hillslope show more scatter and are more likely to be below the steady-state erosion window. (d) Bedrock erosion rates show no correlation with soil thickness.

this hillslope is, therefore, controlled by climate, relict topography, and local baselevel. The channel sample (YH-05-44b, Table II) plots in the complex exposure zone (Figure 11a) and Equations 5 and 7 give significantly different incision rates (1·7 ± 0·5 m Ma^{-1} and 0·15 ± 0·08 m Ma^{-1}, respectively). The ^{26}Al/^{10}Be-derived P would require that the average channel incision over >1 Ma has been ~0·15 m Ma^{-1} (in order to establish the low ^{26}Al/^{10}Be ratio), followed by recent ($\leq$ a few 10^5 a) removal of >70 cm (~one-half an attenuation length if ρ_s = 1·5 g cm^{-3}) of material (to decrease the CRN concentration). This exposure history seems unlikely for two reasons. First, the consistency of P on the active hillslope (Table II) suggests that it is in near adjustment to its boundary condition, which would imply channel incision is ~0·9 m Ma^{-1}. Second, soils thin rapidly towards the channel in some places (H decreases from ~10 to 0 cm, over <30 cm distance), forming small cliffs and indicating possible periodic excavation of material from the channel during rare storm events. Based on a smoothed topographic map, this fill likely did not exceed ~50 cm. This channel fill would cause P calculated with Equation 5 to be too high because the shielding is underestimated. If channel erosion is recalculated using Equation 5, assuming ~50 cm of fill is present most of the time and the ρ_s = 1·5 g cm^{-3}, the revised rate is ~0·7–1·1 m Ma^{-1}. In contrast, the stable hillslope is abutted by Miocene to Holocene alluvium accumulating in an internally-drained basin with localized salar deposits (Marinovic *et al.*, 1992).

On the active hillslope, H increases slightly with distance downslope and averages 5·5 cm (n = 43) (Figure 11b). There are a few places where H is greater, up to 24 cm, and these coincide with rare, hydrothermally-altered zones in the bedrock. Bedrock in these zones is more susceptible to salt intrusion and disintegrates into finer pieces compared to the unaltered bedrock. On the stable hillslope, only seven soils could be excavated to the base of the soil due to the degree of salt cementation and their greater H (average = 57 cm). The retention of atmospheric inputs is likely increased on the gentler stable hillslope by low soil flux (∇z = 0·13 to 0·36, versus 0·34 to 0·65 on the active hillslope) (Figure 4h).

On the active hillslope, P are nearly uniform, ranging from 0·7 to 1·3 m Ma^{-1} regardless of calculation method (Table II) (Figure 11c). Equations 5 and 7 produce similar P values because the ^{26}Al/^{10}Be ratios plot near the steady-state erosion window, within error (Figure 11a). These ratios suggest that the soil on the active hillslope is near steady state ($\partial H/\partial t$ = 0 and $\partial P/\partial t$ = 0), and is near geomorphic steady state (P of the hillslope and channel are the same), despite the extremely slow rates of bedrock erosion and soil development.

On the stable hillslope, P are lower and show no trend with distance downslope (Figure 11c, Table II). The error for many of these samples is large due to difficulties in measuring low ^{26}Al/^{27}Al in the high-Al quartz and the extremely low ^{26}Al/ ^{10}Be ratios of some samples (Figure 11a). Several exposure histories could produce the low ^{26}Al/^{10}Be ratios and relatively high CRN concentrations of the hillslope bedrock. As described earlier, the bedrock has likely experienced erosion at the surface followed by burial by salt and dust. For this exposure history, P values are more accurate with Equation 5 but are overestimates because present-day H is likely greater than past H. Thus, present-day P on the stable hillslope may be near zero under the relatively thick soil.

The ranges of P and H on the active hillslope are narrow, as expected for a hillslope in geomorphic steady state, and cannot be used to test Equation 2 (Figure 11d). Though the stable hillslope has a wider range of H, P are independent of H and have likely experienced non-steady H (Figure 11d). We can only say that on the stable hillslope, where H is much greater than the active hillslope, P may be lower.

In summary, the active hillslope has thinner H and faster P compared to the stable hillslope. This suggests that soil transport is slope-dependent and P is H-dependent, as described earlier. P could not be described as a function of H in the form of Equation 2, but our results suggest there is some H above which P declines. However P values are somewhat slower than on the arid hillslopes and 10 times slower than on the semi-arid hillslopes.

Discussion

Our data reveal systematic changes in soil thickness and the rate of soil production from bedrock due to both boundary

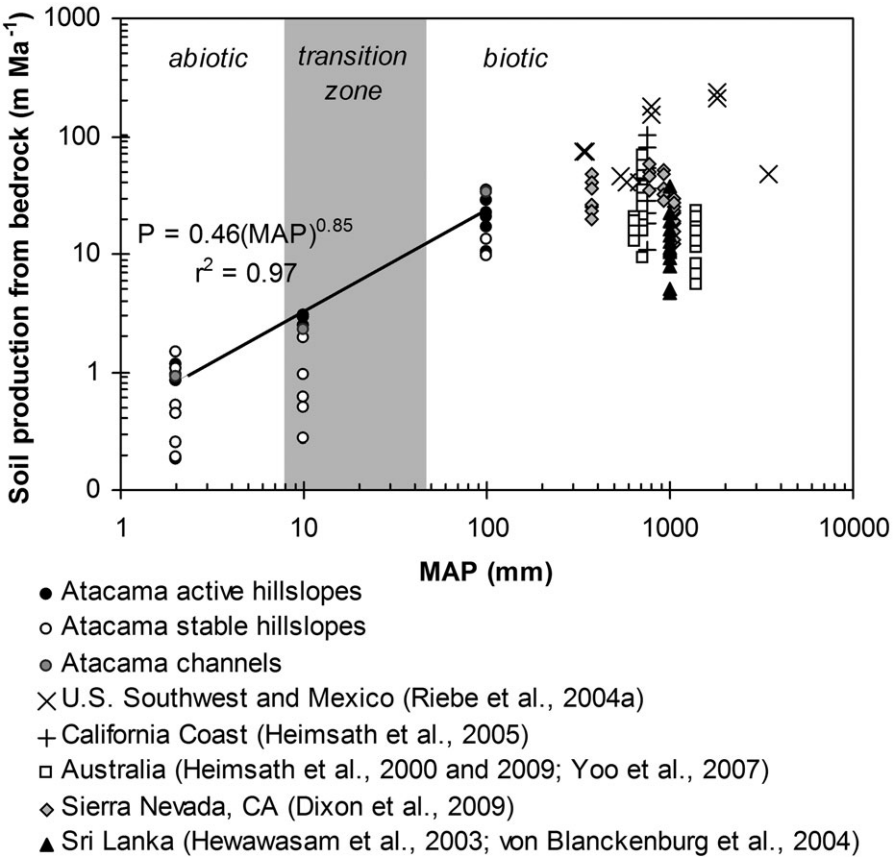

Figure 12. Hillslope bedrock erosion rate as a function of MAP. Data are limited to CRN-derived rates from granitic bedrock at the soil–bedrock interface, except for the Riebe *et al*. (2004a) data which were calculated from hillslope soils. In a well-mixed system, soil production rates calculated from the soil should be similar to rates calculated from bedrock. The black trendline is through the data from active hillslopes in this study. MAT ranges from 11 to 16°C, except for the Riebe *et al*. (2004a) samples which range from 3 to 25°C. Bedrock erosion rates were calculated using Equation 5 except for the stable arid Atacama hillslope which was calculated using Equation 7.

condition and climate. Here we explore the different ways climate affects the hillslope soils and erosion rates and compare our results with those from semi-arid to humid hillslopes. Together, these results define a precipitation-dependent geomorphic threshold.

One complication in interpreting CRN-derived *P* is that they integrate over different timescales depending on *P* (i.e. *P* from the semi-arid hillslopes integrate over ~40 ka, whereas *P* from the hyperarid hillslopes integrate over >600 ka). However, on the active hillslopes CRN concentrations are near steady state, such that most of any inherited CRN signature from an earlier wetter period appears to have been removed. On the stable hillslopes, we used this CRN inheritance to interpret the exposure history of the samples.

Channels at the base of the active hillslopes are incising at rates much slower than local tectonic uplift; the semi-arid channel is incising at less than one-half the local uplift rate, while the arid channel site is above a knickpoint and the hyperarid active channel drains to an internal drainage. Channel incision rates appear to be MAP-limited (Figure 12). As described earlier, channel incision ultimately sets the erosion rate of the hillslope, thus the differences between hillslopes in different climate zones are largely due to the MAP-driven changes in boundary condition, as mediated by soil production and transport processes.

Though consistent differences in *H* with hillslope boundary condition were observed, they were not as large as the variation with MAP (Table I). Average *H* changes non-monotonically with MAP: it is thickest at the hyperarid and semi-arid sites and nearly absent at the arid site (Table I). Soil production and erosion mechanisms change from biotically-driven to salt-driven with decreasing MAP, and this change impacts the soil mass balance. The changes in *P* and *H* appear to be recorded in the low $^{26}Al/^{10}Be$ ratios in the hyperarid hillslope bedrock. This demonstrates the utility of measuring two CRN if non-steady exposure histories are suspected.

The shift from thick and chemically-weathered soils, to nearly bare bedrock, to thick and salty soils with decreasing MAP occurs regardless of boundary condition and demonstrates the profound impact climate has on the development of soils. It also suggests a positive correlation between MAP and *K* (or similar transport coefficient), particularly since hillslope gradients are similar on the active hillslopes. The similarity between the active hillslope *P* and the incision rates of their respective channels supports that channel incision is an important control on *P* and the soil mass balance. If *P* and *H* on the active hillslopes were unable to respond to faster channel incision due to precipitation limitation, topographic discontinuities (bedrock cliffs) would form at the hillslope-channel transition as evidence of geomorphic disequilibrium. Instead, the hillslopes transition smoothly to the channels.

In order to put our results in a global context, *P* calculated using similar methods to ours (i.e. from samples from the soil–bedrock interface) on other non-landsliding, granitic hillslopes were compiled and plotted against MAP (Figure 12). Along the precipitation gradient in this study, *P* increases with increasing MAP following a power law (for active hillslopes $P = 0{\cdot}46(MAP)^{0{\cdot}85}$, $r^2 = 0{\cdot}97$, Figure 12), and the variation between climatic regions is greater than variations within a climatic region (i.e. due to boundary condition). In contrast, for MAP > 100 mm, *P* and MAP are not correlated and *P* varies by an order of magnitude at a given MAP. Our semi-arid data plot within the variance of the data from more humid regions, but our arid and hyperarid data plot significantly below. The source of the variance in *P* is generally attributed to variations in tectonic uplift, though bedrock characteristics and temperature may also be important factors.

At sufficient precipitation other factors (e.g. uplift rates, sediment size and supply, and bedrock resistance) control local channel incision rates, and the response of hillslope soils to these rates is biologically mediated. Biota plays the dual role of

(1) loosening bedrock and dispersing soil downslope, and (2) stabilizing the soil by holding it together by root strength, shielding it from raindrop impacts, and slowing overland flow. Thus, the humid landscapes may record multiple factors effective over various spatial and temporal scales and this produces large variability in *P*. The arid site in this study marks the transition from biotic to abiotic hillslope processes, where soils that are no longer supported by roots are stripped from the hillslope by trampling and rare overland flows. At the extreme, hyperarid channel incision and *P* are controlled primarily by precipitation and perhaps slightly by relict topography.

The surprising discovery here is that increasing aridity, and concurrent decreases in biota, produce systematic and dramatic decreases in channel incision and hillslope bedrock erosion rates. A threshold may exist below which MAP is the dominant control on *P*, and above which other factors (tectonic setting, biota, and/or chemical weathering) dominate.

Conclusions

This work provides the first evidence for precipitation-dependent hillslope bedrock erosion rates and quantifies the effect of boundary condition on hillslope erosion rates and processes. Counter to observations from more humid regions, bedrock erosion rate decreases following a power law as precipitation decreases from semi-arid to hyperarid, and this trend is observed regardless of boundary condition. At our study sites, geomorphic processes shift from relatively fast and biotically-driven in the semi-arid south, to slow and abiotic (salt-driven) in the hyperarid north. Hyperarid hillslopes, with their exceedingly low soil production and soil erosion rates, approach (but do not reach) the role of passive accumulators of atmospheric input. Because the region receives occasional precipitation, soil thickness is still a function of hillslope gradient but rates of soil production from bedrock are largely independent of soil thickness.

The Atacama Desert provides a multi-million year-old experiment testing the effect of water and life on geophysical and geochemical processes. In contrast with portions of the planet where biota modulates soil production and erosion through complex and rapid feedbacks (Yoo *et al*., 2005), the absence of biota in the driest parts of the Atacama Desert results in the rates and mechanisms of geomorphic processes being extremely precipitation-sensitive. This unusual environment, for Earth, illuminates the uniqueness and complexity of a planet whose surface bears the indelible imprint of life.

Acknowledgements—This project was funded by a NASA GSRP #5135, an IGPP LNLL minigrant, and NSF grant # EAR-0447411. Thanks to Sarah Reed for her help with fieldwork, Marc Caffee and Robert Finkel for AMS measurements, and to Kyungsoo Yoo and Arjun Heimsath for discussions of hillslopes.

References

Ahnert F. 1970. Functional relationships between denudation, relief, and uplift in large, mid-latitude drainage basins. *American Journal of Science* **268**: 243–263.

Ahnert F. 1987. Approaches to dynamic equilibrium in theoretical simulations of slope development. *Earth Surface Processes and Landforms* **12**: 3–15.

Alpers CN, Brimhall GH. 1988. Middle Miocene climatic change in the Atacama Desert, Northern Chile – evidence from supergene mineralization at La Escondida. *Geological Society of America Bulletin* **100**: 1640–1656.

Amundson R, Ewing S, Michalski G, Thiemens M, Kendall C, Nishiizumi K, McKay C, Chong G. 2007. The climatic and biotic thresholds on soil elemental cycling along an arid to hyperarid rainfall gradient. *Geochimica et Cosmochimica Acta* **71**: A22–A22.

Anderson RS. 2002. Modeling the tor-dotted crests, bedrock edges, and parabolic profiles of high alpine surfaces of the Wind River Range, Wyoming. *Geomorphology* **46**: 35–58.

Anderson RS, Humphrey NF. 1989. Interaction of weathering and transport processes in the evolution of arid landscapes. *Quantitative Dynamic Stratigraphy* 349–361.

Anderson SP, Dietrich WE, Brimhall GH. 2002. Weathering profiles, mass-balance analysis, and rates of solute loss: linkages between weathering and erosion in a small, steep catchment. *GSA Bulletin* **114**: 1143–1158.

Armstrong AC. 1987. Slopes, boundary conditions, and the development of convexo-concave forms – some numerical experiments. *Earth Surface Processes and Landforms* **12**: 17–30.

Betancourt JL, Latorre C, Rech JA, Quade J, Rylander KA. 2000. A 22,000-year record of monsoonal precipitation from Northern Chile's Atacama Desert. *Science* **289**: 1542–1546.

Böhlke JK, Ericksen GE, Revesz K. 1997. Stable isotope evidence for an atmospheric origin of desert nitrate deposits in northern Chile and southern California, USA. *Chemical Geology* **136**: 135–152.

Braun J, Heimsath AM, Chappell J. 2001. Sediment transport mechanisms on soil-mantled hillslopes. *Geology* **29**: 683–686.

Cáceres L, Gómez-Silva B, Garró X, Rodríguez V, Monardes V, McKay CP. 2007. Relative humidity patterns and fog water precipitation in the Atacama Desert and biological implications. *Journal of Geophysical Research* **112**: G04S14. DOI. 10.1029/2006JG000344

Cardell C, Rivas T, Mosquera M, Birginie J, Moropoulou A, Prieto B, Silva B, Van Grieken R. 2003. Patterns of damage in igneous and sedimentary rocks under conditions simulating sea-salt weathering. *Earth Surface Processes and Landforms* **28**: 1–14.

Carson MA, Kirkby MJ. 1972. *Hillslope Form and Process*. Cambridge University Press: Cambridge.

Clarke JDA. 2006. Antiquity of aridity in the Chilean Atacama Desert. *Geomorphology* **73**: 101–114.

Coppus R, Imeson AC. 2002. Extreme events controlling erosion and sediment transport in a semi-arid sub-Andean valley. *Earth Surface Processes and Landforms* **27**: 1365–1375.

Dahlgren RA, Boettinger JL, Huntington GL, Amundson RG. 1997. Soil development along an elevational transect in the western Sierra Nevada, California. *Geoderma* **78**: 207–236.

Dietrich WE, Reiss R, Hsu ML, Montgomery DR. 1995. A process-based model for colluvial soil depth and shallow landsliding using digital elevation data. *Hydrological Processes* **9**: 383–400.

Dietrich WE, Bellugi DG, Sklar LS, Stock JD, Heimsath AM, Roering JJ. 2003. Geomorphic transport laws for predicting landscape form and dynamics; prediction in Geomorphology. *Geophysical Monograph* **135**: 103–132.

Dietrich WE, Perron JT. 2006. The search for a topographic signature of life. *Nature* **439**: 411–418.

Dixon JL, Heimsath AM, Amundson R. 2009. The critical role of climate and saprolite weathering in landscape evolution. *Earth Surface Processes and Landforms* **34**(11): 1507–1521. DOI: 10.1002/esp.1836.

Dunai TJ, Gonzalez-Lopez GA, Juez-Larre J, Carrizo D. 2005. Preservation of (early) Miocence landscapes in the Atacama Desert, northern Chile. *Geochimica et Cosmochimica Acta* **69**: A161–A161.

Emparan C, Pineda G. 2000. *La Serena – La Higuera. Region de Coquimbo. Servicio Nacional de Geología y Minería*, Geologic map No. 18, 1:100,000, Santiago.

Encinas A, Hervé F, Villa-Martínez R, Nielsen SN, Finger KL, Peterson DE. 2006. Finding of a Holocene marine layer in Algarrobo (33° 22′ S), central Chile. Implications for coastal uplift. *Revista Geologica de Chile* **33**: 339–345.

Ericksen GE. 1981. *Geology and Origin of the Chilean Nitrate Deposits*, Geological Society Professional Paper 1188. United States Government Printing Office: Washington, DC.

Evenstar LA, Hartley AJ, Stuart FM, Mather AE, Rice CM, Chong G. 2009. Multiphase development of the Atacama Planation Surface recorded by cosmogenic ^{3}He exposure ages: Implications for uplift

and Cenozoic climate change in western South America. *Geology* **37**: 27–30.

Ewing S, Michalski G, Thiemens M, Quinn R, Macalady J, Kohl S, Wankel S, Kendall C, McKay CP, Amundson R. 2007. Rainfall limit of the N cycle on Earth. *Global Biogeochemical Cycles* **21**: GB3009.

Ewing SA, Sutter B, Owen JJ, Nishiizumi K, Sharp W, Cliff SS, Perry K, Dietrich WE, McKay CP, Amundson R. 2006. A threshold in soil formation at Earth's arid-hyperarid transition. *Geochimica et Cosmochimica Acta* **70**: 5293–5322.

Fernandes NF, Dietrich WE. 1997. Hillslope evolution by diffusive processes: the timescale for equilibrium adjustments. *Water Resources Research* **33**: 1307–1318.

Fleming RW, Johnson AM. 1975. Rates of seasonal creep of silty clay soil. *The Quarterly Journal of Engineering Geology* **8**: 1–29.

Furbish DJ. 2003. Using the dynamically coupled behavior of land-surface geometry and soil thickness in developing and testing hillslope evolution models. *Prediction in Geomorphology* 169–181.

Furbish DJ, Fagherazzi S. 2001. Stability of creeping soil and implications for hillslope evolution. *Water Resources Research* **37**: 2607–2618.

Gabet EJ, Reichman OJ, Seabloom EW. 2003. The effects of bioturbation on soil processes and sediment transport. *Annual Review of Earth and Planetary Sciences* **31**: 249–73.

Gilbert GK. 1877. *Geology of the Henry Mountains (Utah), U.S. Geographical and Geological Survey of the Rocky Mountains Region*. US Geological Survey: Washington, DC.

Godoy E, Lara L. 1998. *Hojas Chañaral y Diego de Almagro, Región de Atacama. Servicio Nacional de Geología y Minería*, Geologic map of Chile No. 5–6, 1:100,000, Santiago.

Grocott J, Taylor GK. 2002. Magmatic arc fault systems, deformation partitioning and emplacement of granitic complexes in the Coastal Cordillera, north Chilean Andes (25°30'S to 27°00'S). *Journal of the Geological Society* **159**: 425–442.

Hartley AJ, Chong G. 2002. Late Pliocene age for the Atacama Desert: implications for the desertification of western South America. *Geology* **30**: 43–46.

Hartley AJ, Chong G, Houston J, Mather AE. 2005. 150 million years of climatic stability: evidence from the Atacama Desert, northern Chile. *Journal of the Geological Society* **162**: 421–424.

Hebbeln D, Lamy F, Mohtadi M, Echtler H. 2007. Tracing the impact of glacial–interglacial climate variability on erosion of the southern Andes. *Geology* **35**: 131–134.

Heimsath AM, Dietrich WE, Nishiizumi K, Finkel RC. 1997. The soil production function and landscape equilibrium. *Nature* **388**: 358–361.

Heimsath AM, Dietrich WE, Nishiizumi K, Finkel RC. 1999. Cosmogenic nuclides, topography, and the spatial variation of soil depth. *Geomorphology* **27**: 151–172.

Heimsath AM, Chappell J, Dietrich WE, Nishiizumi K, Finkel RC. 2000. Soil production on a retreating escarpment in southeastern Australia. *Geology* **28**: 787–790.

Heimsath AM, Chappell J, Finkel RC, Fifield K, Alimanovic A. 2006. Escarpment erosion and landscape evolution in southeastern Australia. In *Tectonics, Climate, and Landscape Evolution*, Willett SD, Hovius N, Brandon MT, Fisher DM (eds), Geological Society of America Special Paper 398, Penrose Conference Series. The Geological Society of America: Boulder, CO; 173–190.

Heimsath AM, Furbish DJ, Dietrich WE. 2005. The illusion of diffusion: field evidence for depth-dependent sediment transport. *Geology* **33**: 949–952.

Heimsath AM, Chappell J, Hancock GR, Fink D, Fifield K. 2008. Eroding Australia: slowly. *Geochemica Cosmochemica Acta* **72**: A363.

Heimsath AM, Fink D, Hancock GR. 2009. The 'humped' soil production function: eroding Arnhem Land, Australia. *Earth Surface Processes and Landforms* **34**: 1674–1684.

Hewawasen T. 2003. *Quantifying erosion in the tropical highlands of Sri Lanka over different time scales using cosmogenic nuclide and river load data*. Ph.D. thesis, University of Bern: Bern, Switzerland.

Houston J. 2006. Variability of precipitation in the Atacama desert: its causes and hydrological impact. *International Journal of Climatology* **26**: 2181–2198.

Jackson D, Méndez C, Seguel R, Maldonado A, Vargas G. 2007. Initial occupation of the Pacific Coast of Chile during Late Pleistocene times. *Current Anthropology* **48**: 725–731.

Jenny H. 1941. *Factors of Soil Formation*. McGraw-Hill Book Company: New York.

Kalthoff N, Fiebig-Wittmaack M, Meissner C, Kohler M, Uriarte M, Bischoff-Gauss I, Gonzales E. 2006. The energy balance, evapotranspiration and nocturnal dew deposition of an arid valley in the Andes. *Journal of Arid Environments* **65**: 420–443.

Kirkby MJ. 1967. Measurement and theory of soil creep. *Journal of Geology* **75**: 359–378.

Kirkby MJ. 1971. Hillslope process-response models based on the continuity equation. *Institute of British Geographers Special Publication* **3**: 15–30.

Kober F, Ivy-Ochs S, Schlunegger F, Baur H, Kubik PW, Wieler R. 2007. Denudation rates and a topography-driven rainfall threshold in northern Chile: multiple cosmogenic nuclide data and sediment yield budgets. *Geomorphology* **83**: 97–120.

Kohl CP, Nishiizumi K. 1992. Chemical isolation of quartz for measurement of *in situ*-produced cosmogenic nuclides. *Geochimica et Cosmochimica Acta* **56**: 3583–3587.

Lal D. 1991. Cosmic-ray labeling of erosion surfaces – *in situ* nuclide production-rates and erosion models. *Earth and Planetary Science Letters* **104**: 424–439.

Lal D, Arnold JR. 1985. Tracing quartz through the environment. *Proceedings of the Indian Academy of Science (Earth Planetary Science Section)* **94**: 1–5.

Lamy F, Klump J, Hebbeln D, Wefer G. 2000. Late Quaternary rapid climate change in northern Chile. *Terra Nova* **12**: 8–13.

Latorre C, Betancourt JL, Rylander KA, Quade J. 2002. Vegetation invasions into absolute desert: a 45 000 yr rodent midden record from the Calama-Salar de Atacama basins, northern Chile (lat 22°–24°S). *Geological Society of America Bulletin* **114**: 349–366.

Latorre C, Betancourt JL, Rylander KA, Quade J, Matthei O. 2003. A vegetation history from the arid prepuna of northern Chile (22–23° S) over the last 13,500 years. *Palaeogeography, Palaeoclimatology, Palaeoecology* **194**: 223–246.

Lebedeva MI, Fletcher RC, Brantley SL. 2010. A mathematical model for steady-state regolith production at constant erosion rate. *Earth Surface Processes and Landforms* **35**: 508–524.

Le Roux JP, Gomez C, Venegas C, Fenner J, Middleton H, Marchant M, Buchbinder B, Frassinetti D, Marquardt C, Gregory-Wodzicki KM, Lavenu A. 2005. Neogene-Quaternary coastal and offshore sedimentation in north central Chile: record of sea-level changes and implications for Andean tectonism. *Journal of South American Earth Sciences* **19**: 83–98. DOI. 10.1016/j.jsames.2003.11.003

Le Roux JP, Olivares DM, Nielsen SN, Smith ND, Middleton H, Fenner J, Ishman SE. 2006. Bay sedimentation as controlled by regional crustal behavior, local tectonics and eustatic sea-level changes: Coquimbo Formation (Miocene-Pliocene), Bay of Tongoy, central Chile. *Sedimentary Geology* **184**: 133–153. DOI. 10.1016/j.sedgeo.2005.09.023

Leonard EM, Wehmiller JF. 1992. Low uplift rates and terrace reoccupation inferred from mollusk aminostratigraphy, Coquimbo Bay area, Chile. *Quaternary Research* **38**: 246–259.

Loveless JP, Hoke GD, Allmendinger RW, Gonzalez G, Isacks BL, Carrizo DA. 2005. Pervasive cracking of the northern Chilean Coastal Cordillera: new evidence for forearc extension. *Geology* **33**: 973–976.

Marinovic N, Smoje I, Maksaev V, Hervé M, Mpodozis C. 1992. *Hoja Aguas Blancas, Región de Antofagasta*, Servicio Nacional de Geología y Minería, Geologic map of Chile No. 70, 1:100,000, Santiago.

Marquardt C, Lavenu A, Ortlieb L, Godoy E, Comte D. 2004. Coastal neotectonics in Southern Central Andes: uplift and deformation of marine terraces in Northern Chile (27°S). *Tectonophysics* **394**: 193–219.

McKay CP, Friedmann EI, Gomez-Silva B, Caceres-Villanueva L, Andersen DT, Landheim R. 2003. Temperature and moisture conditions for life in the extreme arid region of the Atacama Desert: four years of observations including the El Niño of 1997–1998. *Astrobiology* **3**: 393–406.

Michalski G, Böhlke J, Thiemens M. 2004. Long term atmospheric deposition as the source of nitrate and other salts in the Atacama Desert, Chile: new evidence from mass-independent oxygen isotopic compositions. *Geochimica et Cosmochimica Acta* **68**: 4023–4038.

Molnar P, Anderson RS, Anderson SP. 2007. Tectonics, fracturing of rock, and erosion. *Journal of Geophysical Research – Earth Surface* **112**: F03014.

Montgomery DR, Balco G, Willett SD. 2001. Climate, tectonics, and the morphology of the Andes. *Geology* **29**: 579–582.

Mortimer C. 1973. The Cenozoic history of the southern Atacama Desert, Chile. *Journal of the Geological Society of London* **129**: 505–526.

Mortimer C. 1980. Drainage evolution in the Atacama Desert of northern Chile. *Revista Geológica de Chile* **11**: 3–28.

Mostny G. 1972. *Prehistoria de Chile*. Editorial Universitaria: Santiago.

Mudd SM, Furbish DJ. 2004. Influence of chemical denudation on hillslope morphology. *Journal of Geophysical Research – Earth Surface* **109**: F02001.

Mudd SM, Furbish DJ. 2007. Responses of soil-mantled hillslopes to transient channel incision rates. *Journal of Geophysical Research – Earth Surface* **112**: F02S18.

Navarro-González R, Rainey F, Molina P, Bagaley D, Hollen B, de la Rosa J, Small A, Quinn R, Grunthaner F, Cáceres L, Gomez-Silva B, McKay CP. 2003. Mars-like soils in the Atacama Desert, Chile, and the dry limit of microbial life. *Science* **302**: 1018–1021.

Nester PL. 2008. *Basin and paleoclimate evolution of the Pampa del Tamargual forearc valley, Atacama Desert, Northern Chile*, PhD Thesis, Cornell University, New York.

Nishiizumi K. 2003. Preparation of ^{26}Al AMS standards. *Nuclear Instruments & Methods in Physics Research Section B* **B223–224**: 388–392.

Nishiizumi K, Winterer EL, Kohl CP, Klein J. 1989. Cosmic ray production rates of ^{10}Be and ^{26}Al in quartz from glacially polished rocks. *Journal of Geophysical Research* **94**: 17907–17915.

Nishiizumi K, Kohl CP, Arnold JR, Klein J, Fink D, Middleton R. 1991. Cosmic ray produced ^{10}Be and ^{26}Al in Antarctic rocks: exposure and erosion history. *Earth and Planetary Science Letters* **104**: 440–454.

Nishiizumi K, Caffee MW, Finkel RC, Brimhall G, Mote T. 2005. Remnants of a fossil alluvial fan landscape of Miocene age in the Atacama Desert of northern Chile using cosmogenic nuclide exposure age dating. *Earth and Planetary Science Letters* **237**: 499–507.

Nishiizumi K, Imamura M, Caffee MW, Southon JR, Finkel RC, McAninch J. 2007. Absolute calibration of ^{10}Be AMS standards. *Nuclear Instruments & Methods in Physics Research Section B* **258**: 403–413.

Oberlander TM. 1972. Morphogenesis of granitic boulder slopes in Mojave Desert, California. *Journal of Geology* **80**: 1–20.

Onda Y. 1992. Influence of water storage capacity in the regolith zone on hydrological characteristics, slope processes, and slope form. *Zeitschrift Fur Geomorphologie* **36**: 165–178.

Ortlieb L, Zazo C, Goy JL, Hillaire-Marcel C, Ghaleb B, Cournoyer L. 1996. Coastal deformation and sea-level changes in the northern Chile subduction area (23°S) during the last 330 ky. *Quaternary Science Reviews* **15**: 819–831.

Ota Y, Miyauchi T, Paskoff R, Koba M. 1995. Plio-Quaternary marine terraces and their deformation along the Altos de Talinay, North-Central Chile. *Revista Geológica de Chile* **22**: 89–102.

Pérez Valdivia CA. 2005. *Cambio climático: Vulnerabilidad, adaptación y rol institucional. Estudio de casos en el Valle de Elqui*, PhD Thesis, Universidad de La Serena.

Placzek C, Matmon A, Granger D, Quade J, Niedermann S. 2010. Evidence for active landscape evolution in the hyperarid Atacama from multiple terrestrial cosmogenic nuclides. *Earth and Planetary Science Letters* **295**: 12–20.

Quezada J, González G, Dunai T, Jensen A, Juez-Larré J. 2007. Pleistocene littoral uplift of northern Chile: Ne-21 age of the upper marine terrace of Caldera-Bahia Inglesa area. *Revista Geologica de Chile* **34**: 81–96.

Ravelo AC, Andreasen DH, Lyle M, Lyle AO, Wara MW. 2004. Regional climate shifts caused by gradual global cooling in the Pliocene epoch. *Nature* **429**: 263–267.

Rech J, Quade J, Hart W. 2003. Isotopic evidence for the source of Ca and S in soil gypsum, anhydrite and calcite in the Atacama Desert, Chile. *Geochimica et Cosmochimica Acta* **67**: 575–586.

Riebe CS, Kirchner JW, Granger DE, Finkel RC. 2001. Strong tectonic and weak climatic control of long-term chemical weathering rates. *Geology* **29**: 511–514.

Riebe CS, Kirchner JW, Finkel RC. 2004a. Erosional and climatic effects on long-term chemical weathering rates in granitic landscapes spanning diverse climate regimes. *Earth and Planetary Science Letters* **224**: 547–562.

Riebe CS, Kirchner JW, Finkel RC. 2004b. Sharp decrease in long-term chemical weathering rates along an altitudinal transect. *Earth and Planetary Science Letters* **218**: 421–434.

Rodriguez-Navarro C, Doehne E. 1999. Salt weathering: Influence of evaporation rate, supersaturation and crystallization pattern. *Earth Surface Processes and Landforms* **24**: 191–209.

Roering JJ. 2008. How well can hillslope evolution models 'explain' topography? Simulating soil transport and production with high-resolution topographic data. *Geological Society of America Bulletin* **120**: 1248–1262.

Roering JJ, Kirchner JW, Dietrich WE. 1999. Evidence for nonlinear, diffusive sediment transport on hillslopes and implications for landscape morphology. *Water Resources Research* **35**: 853–870.

Rundel PW, Dillon MO, Palma B, Mooney HA, Gulmon SL, Ehleringer JR. 1991. The phytogeography and ecology of the coastal Atacama and Peruvian deserts. *Aliso* **13**: 1–49.

Rundel PW, Dillon MO, Palma P. 1996. Flora and vegetation of Pan de Azucar National Park in the Atacama Desert of northern Chile. *Gayana Botánica* **53**: 295–315.

Saillard M, Hall SR, Audin L, Farber DL, Herail G, Martinod J, Regard V, Finkel RC, Bondoux F. 2009. Non-steady long-term uplift rates and Pleistocene marine terrace development along the Andean margin of Chile (31°S) inferred from Be-10 dating. *Earth and Planetary Science Letters* **277**: 50–63.

Schoenenberger PJ, Wysocki DA, Benham EC, Broderson WD. 2002. *Field Book for Describing and Sampling Soils*. Natural Resources Conservation Service, National Soil Survey Center: Lincoln, NE.

Selby MJ. 1980. A rock mass strength classification for geomorphic purposes: with tests from Antarctica and New Zealand. *Zeitschrift für Geomorphologie* **24**: 31–51.

Sillitoe RH, McKee EH. 1996. Age of supergene oxidation and enrichment in the Chilean porphyry copper province. *Economic Geology and the Bulletin of the Society of Economic Geologists* **91**: 164–179.

Small EE, Anderson RS, Hancock GS. 1999. Estimates of the rate of regolith production using ^{10}Be and ^{26}Al from an alpine hillslope. *Geomorphology* **27**: 131–150.

Squeo FA, Aravena R, Aguirre E, Pollastri A, Jorquera CB, Ehleringer JR. 2006. Groundwater dynamics in a coastal aquifer in north-central Chile: implications for groundwater recharge in an arid ecosystem. *Journal of Arid Environments* **67**: 240–254.

Steiger M. 2005. Crystal growth in porous materials – I: the crystallization pressure of large crystals. *Journal of Crystal Growth* **282**: 455–469.

Vargas G, Rutllant J, Ortlieb L. 2006. ENSO tropical-extratropical climate teleconnections and mechanisms for Holocene debris flows along the hyperarid coast of western South America (17°–24° S). *Earth and Planetary Science Letters* **249**: 467–483.

Viles H, Goudie A. 2007. Rapid salt weathering in the coastal Namib Desert: implications for landscape development. *Geomorphology* **85**: 49–62.

von Blanckenburg F. 2006. The control mechanisms of erosion and weathering at basin scale from cosmogenic nuclides in river sediment. *Earth and Planetary Science Letters* **242**: 223–239.

von Blanckenburg F, Hewawasam T, Kubik PW. 2004. Cosmogenic nuclide evidence for low weathering and denudation in the wet, tropical highlands of Sri Lanka. *Journal of Geophysical Research* **109**: F03008. doi:10.1029/2003JF000049.

Warren-Rhodes K, Rhodes K, Pointing S, Ewing S, Lacap D, Gomez-Silva B, Amundson R, Friedmann E, McKay C. 2006. Hypolithic

cyanobacteria, dry limit of photosynthesis, and microbial ecology in the hyperarid Atacama Desert. *Microbial Ecology* **52**: 389–398.

Wheeler JC. 1995. Evolution and present situation of the South-American *Camelidae*. *Biological Journal of the Linnean Society* **54**: 271–295.

Wilkinson MT, Humphreys GS. 2005. Exploring pedogenesis via nuclide-based soil production rates and OSL-based bioturbation rates. *Australian Journal of Soil Research* **43**: 767–779.

Winkler E, Singer P. 1972. Crystallization pressure of salts in stone and concrete. *Geological Society of America Bulletin* **83**: 3509–3513.

Wobus CW, Crosby BT, Whipple KX. 2006. Hanging valleys in fluvial systems: controls on occurrence and implications for landscape evolution. *Journal of Geophysical Research – Earth Surface*: **111**: F02017.

Yoo K, Amundson R, Heimsath AM, Dietrich WE. 2005. Process-based model linking pocket gopher (*Thomomys bottae*) activity to sediment transport and soil thickness. *Geology* **33**: 917–920.

Yoo K, Amundson R, Heimsath AM, Dietrich WE, Brimhall GH. 2007. Integration of geochemical mass balance with sediment transport to calculate rates of soil chemical weathering and transport on hillslopes. *Journal of Geophysical Research – Earth Surface*: **112**: F02013.